REPORT DOCUMENTATION PAGE

Form Approved OMB NO. 0704-0188

1. REPORT DATE (DD-MM-YYYY)	2. REPORT TYPE	3. DATES COVERED (From - To)
12-07-2012	Final Report	15-Nov-2006 - 14-Nov-2011

4. TITLE AND SUBTITLE

Investigations of tissue-level mechanisms of primary blast injury through modeling, simulation, neuroimaging and neuropathological studies

5a. CONTRACT NUMBER
W911NF-07-1-0035

5b. GRANT NUMBER

5c. PROGRAM ELEMENT NUMBER
121000

6. AUTHORS

R. Radovitzky

5d. PROJECT NUMBER

5e. TASK NUMBER

5f. WORK UNIT NUMBER

7. PERFORMING ORGANIZATION NAMES AND ADDRESSES

Massachusetts Institute of Technology (MIT)
Office of Sponsored Programs
Bldg. E19-750
Cambridge, MA 02139 -4307

8. PERFORMING ORGANIZATION REPORT NUMBER

9. SPONSORING/MONITORING AGENCY NAME(S) AND ADDRESS(ES)

U.S. Army Research Office
P.O. Box 12211
Research Triangle Park, NC 27709-2211

10. SPONSOR/MONITOR'S ACRONYM(S)
ARO

11. SPONSOR/MONITOR'S REPORT NUMBER(S)
51467-EG-JDO.20

12. DISTRIBUTION AVAILIBILITY STATEMENT

Approved for Public Release; Distribution Unlimited

13. SUPPLEMENTARY NOTES

The views, opinions and/or findings contained in this report are those of the author(s) and should not contrued as an official Department of the Army position, policy or decision, unless so designated by other documentation.

14. ABSTRACT

Traumatic brain injury (TBI) to U.S. soldiers has become one of the most taxing consequences of IED attacks in OEF/OIF. This project has focused on investigations of traumatic injury to the brain caused by the primary effects of blast waves. The project combines clinical, experimental and modeling studies aimed at: (i) elucidating the cell and tissue-level mechanisms of injury produced by the effect of the blast wave, (ii) deriving associated blast

15. SUBJECT TERMS

blast, TBI

16. SECURITY CLASSIFICATION OF:			17. LIMITATION OF ABSTRACT	15. NUMBER OF PAGES	19a. NAME OF RESPONSIBLE PERSON
a. REPORT	b. ABSTRACT	c. THIS PAGE			Raul Radovitzky
UU	UU	UU	UU		19b. TELEPHONE NUMBER: 617-252-1518

Report Title

Investigations of tissue-level mechanisms of primary blast injury through modeling, simulation, neuroimaging and neuropathological studies

ABSTRACT

Traumatic brain injury (TBI) to U.S. soldiers has become one of the most taxing consequences of IED attacks in OEF/OIF. This project has focused on investigations of traumatic injury to the brain caused by the primary effects of blast waves. The project combines clinical, experimental and modeling studies aimed at: (i) elucidating the cell and tissue-level mechanisms of injury produced by the effect of the blast wave, (ii) deriving associated blast injury criteria (metrics and thresholds), (iii) helping to identify and treat returnees suffering from TBI, and (iv) developing blast protection strategies for TBI mitigation.

This report summarizes all the main findings and results of the project, including resulting products and deliverables.

Enter List of papers submitted or published that acknowledge ARO support from the start of the project to the date of this printing. List the papers, including journal references, in the following categories:

(a) Papers published in peer-reviewed journals (N/A for none)

Received Paper

TOTAL:

Number of Papers published in peer-reviewed journals:

(b) Papers published in non-peer-reviewed journals (N/A for none)

Received Paper

TOTAL:

Number of Papers published in non peer-reviewed journals:

(c) Presentations

all publications have been reported in previous reports. There were no additional publications in the period 7/31/2011, 11/14/2011.

Number of Presentations: 0.00

Non Peer-Reviewed Conference Proceeding publications (other than abstracts):

Received Paper

TOTAL:

Number of Non Peer-Reviewed Conference Proceeding publications (other than abstracts):

Peer-Reviewed Conference Proceeding publications (other than abstracts):

Received	Paper

TOTAL:

Number of Peer-Reviewed Conference Proceeding publications (other than abstracts):

(d) Manuscripts

Received	Paper

TOTAL:

Number of Manuscripts:

Books

Received	Paper

TOTAL:

Patents Submitted

Patents Awarded

Awards

no additional honors or awards

Graduate Students

NAME	PERCENT_SUPPORTED	Discipline
Michelle Nyein	1.00	
FTE Equivalent:	**1.00**	
Total Number:	**1**	

Names of Post Doctorates

NAME	PERCENT_SUPPORTED
FTE Equivalent:	
Total Number:	

Names of Faculty Supported

NAME	PERCENT_SUPPORTED
FTE Equivalent:	
Total Number:	

Names of Under Graduate students supported

NAME	PERCENT SUPPORTED

FTE Equivalent:

Total Number:

Student Metrics

This section only applies to graduating undergraduates supported by this agreement in this reporting period

The number of undergraduates funded by this agreement who graduated during this period:	0.00
The number of undergraduates funded by this agreement who graduated during this period with a degree in science, mathematics, engineering, or technology fields:.....	0.00
The number of undergraduates funded by your agreement who graduated during this period and will continue to pursue a graduate or Ph.D. degree in science, mathematics, engineering, or technology fields:.....	0.00
Number of graduating undergraduates who achieved a 3.5 GPA to 4.0 (4.0 max scale):	0.00
Number of graduating undergraduates funded by a DoD funded Center of Excellence grant for Education, Research and Engineering:	0.00
The number of undergraduates funded by your agreement who graduated during this period and intend to work for the Department of Defense	0.00
The number of undergraduates funded by your agreement who graduated during this period and will receive scholarships or fellowships for further studies in science, mathematics, engineering or technology fields:	0.00

Names of Personnel receiving masters degrees

NAME

Total Number:

Names of personnel receiving PHDs

NAME

Total Number:

Names of other research staff

NAME	PERCENT SUPPORTED

FTE Equivalent:

Total Number:

Sub Contractors (DD882)

Inventions (DD882)

Scientific Progress

See report attached summarizing major advances in this project. The particular period covered by this report is only four months which did not lead to major advances.

Technology Transfer

Final Report for Agreement Number: W911NF-07-1-0035
Project Title: Investigations of tissue-level mechanisms of primary blast injury through modeling, simulation, neuroimaging and neuropathological studies
Reporting period: August 01, 2011 – November 14, 2012

R. Radovitzky (Principal Investigator)
S. Socrate
Massachusetts Institute of Technology

K. Taber
R. Hurley
VA Salisbury, NC

David Moore
Defense and Veterans Brain Injury Center
Walter Reed Army Medical Center

Steve Son
Wayne Chen
Purdue University

James Deshler
Boston University

Ghatu Subhash
University of Florida

Cameron Bass
Duke University

July 10, 2012

Abstract

Traumatic brain injury (TBI) to U.S. soldiers has become one of the most taxing consequences of IED attacks in OEF/OIF. This project has focused on investigations of traumatic injury to the brain caused by the primary effects of blast waves. The project combines clinical, experimental and modeling studies aimed at: (i) elucidating the cell and tissue-level mechanisms of injury produced by the effect of the blast wave, (ii) deriving associated blast injury criteria (metrics and thresholds), (iii) helping to identify and treat returnees suffering from TBI, and (iv) developing blast protection strategies for TBI mitigation.

This report summarizes all the main findings and results of the project, including resulting products and deliverables.

Contents

1 Background

This project endeavored to conduct basic research studies of blast-induced Traumatic Brain Injury which has become the most significant and at the same time controverislal type of injury sustained by the U.S. warfighter in the OEF/OIF conflicts due to IED attacks.

The project focused on two main aspects of the problem: 1) the physical dimension, which includes the description of the blast event, the propagation of the blast wave and its interaction with the human head with and without protective gear (ACH) and the mechanical response of human tissues and cells to the physical insult, 2) the biological response of the neuron cells resulting from the physical threat.

In the first area, the efforts concentrated on developing advanced simulation tools to describe the coupled interactions between the blast and the head with and without protection. The physical characterization of the blast event, in turn, informs studies of the biological response of the tissue and cell. In addition, high-fidelity simulations conducted with the tools developed are used to analyze the effect of protective head gear in mitigating the intensity of the stress waves reaching the brain tissue, and to explore mitigation strategies beyond those afforded by the existing ACH. In the second area, studies were conducted of the synaptic, ATP and proteomic response of mammal neuron cells in culture subjected to mechanical events.

2 Key results, findings and deliverables of the project

In the following we provide a list of the main results, findings and deliverables of the project:

Deliverables

1. The signature deliverable of this project is the Full Head Model, a biofidelic computational finite element mesh of a human head developed as a project collaboration between Dr. Moore from the Defense and Veterans Brain Injury Center and Prof. Radovitzky at the MIT Institute for Soldier Nanotechnology.

Figure 1 shows a rendering of the original MIT/DVBIC Full Head Model, [2]. The model is based on a careful segmentation of high-resolution MRI images of a human head. Eleven (11) different anatomical structures were differentiated including: fat, skin, muscle, skull, sinus structures, CSF, gray and white matter, venous structures, glia and ventricles. The raw data set was then converted to a solid model, which is subsequently used as input to the mesh generation tool for creating the tetrahedral volume mesh. The resulting meshes usually suffer from severely poor element quality and are unusable for computational simulations.

The figure also shows the addition of a model of the Advanced Combat Helmet (ACH) and padding system. The solid model was merged with the FHM model and the meshing procedure outlined above was followed to obtain a computational mesh. Snapshots with external and internal details of the solid model and resulting mesh are shown in Figure 1. The model has been transitioned to a number of DoD organizations including the Army Research Laboratory, PEO Soldier and the Office of Naval Research. In addition, the model has been publicly released to academic organizations (with careful accounting and consideration of requesting parties and purposes of model use).

2. Another very important deliverable of this project is a general constitutive modeling framework for describing the rate-dependent viscoelastic stress-strain response of different brain tissues [4, 5] and neuron cells [1], Figure 2. The model has been shown to describe the tissue response with a single set of eight model parameters, against in vitro porcine and bovine test data under a wide range of strain rates $10^{-1} - 10^{3} \cdot s^{-1}$ obtained as part of this project [3], Figure 3, as well as in in vivo conditions [5], Figure 4.

Findings Three fundamental findings have resulted from this project:

1. that the conditions the brain is subjected to for a blast event compatible with the threshold for lung injury are well in excess of the threshold values of the accepted brain injury criteria for impact conditions. *This was the first theoretical proof that the primary effects of a blast constitute a plausible cause for mild TBI.*

2. that *the existing Advanced Combat Helmet (ACH) is a safe device under blast loads*, i.e. that it does not exacerbate the blast overpressure on the human head as it had been previously suggested. Given the importance of this finding at the Government level and in the public opinion, I was invited to brief the Professional Staff at the Senate Armed Services Committee.

3. that the most effective strategy to mitigate blast injuries to the brain is to cover the exposed areas of the face to the blast wave, e.g. with a face shield. These findings were also published in the PNAS paper and elicited significant media attention in leading national and international TV, radio, printed and online press.

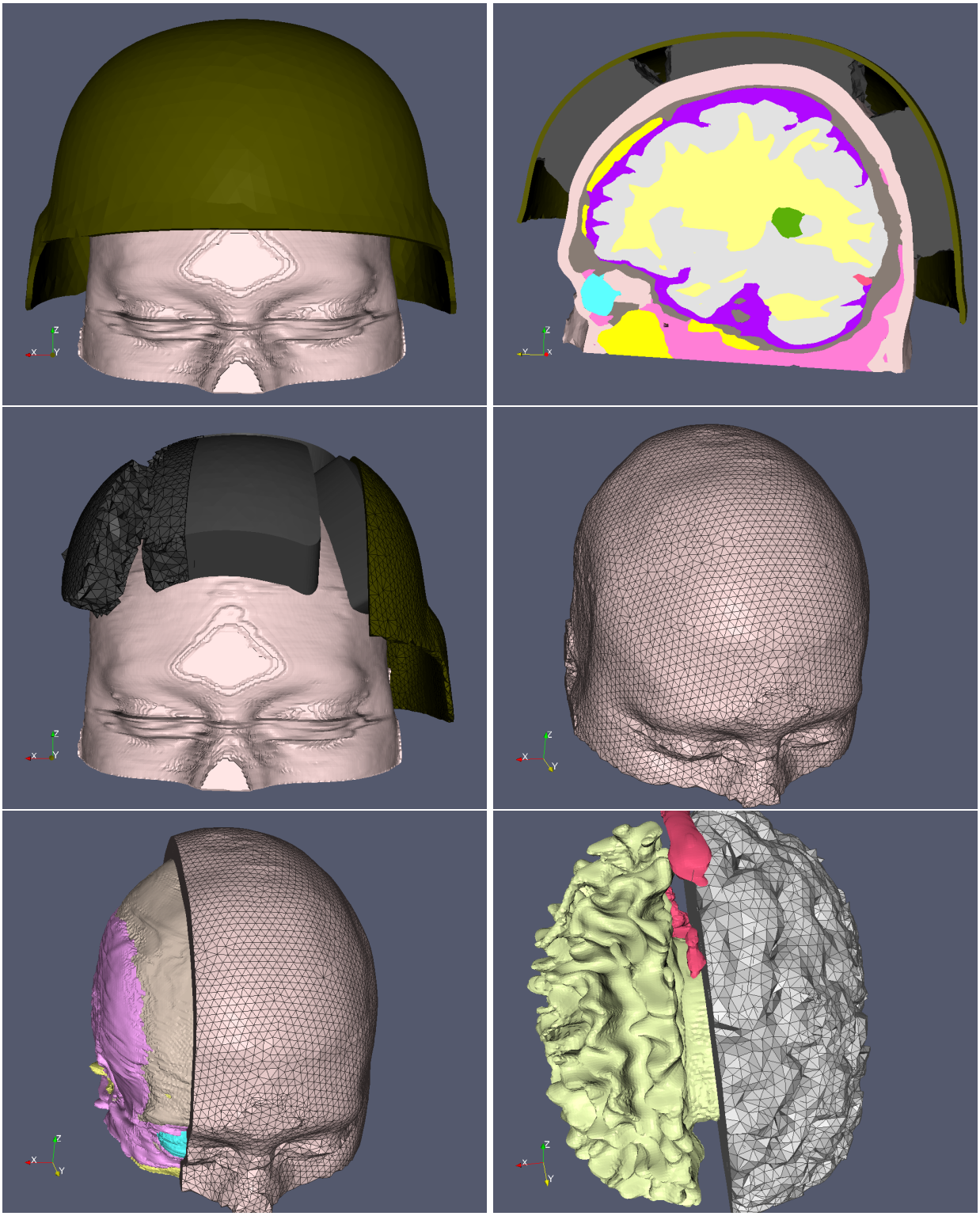

Figure 1: Extension of the Full Head Model (FHM) to include ACH helmet and standard padding system. The figure shows external and internal views of the solid model and finite element mesh

Brain Tissue Properties characterization and modeling: Socrate, Chen, Subhash

- Develop tissue-specific constitutive models
- Consider all relevant response mechanisms: nonlinear visco and poro elasticity, anisotropy, rate-dependency
- In vivo and in vitro tissue characterization of mammal tissue
- Wide range of strain rates

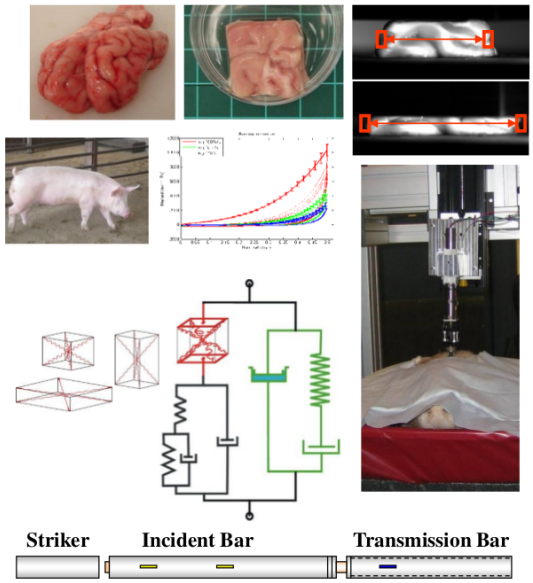

Figure 2: Tissue and Cell constitutive modeling framework

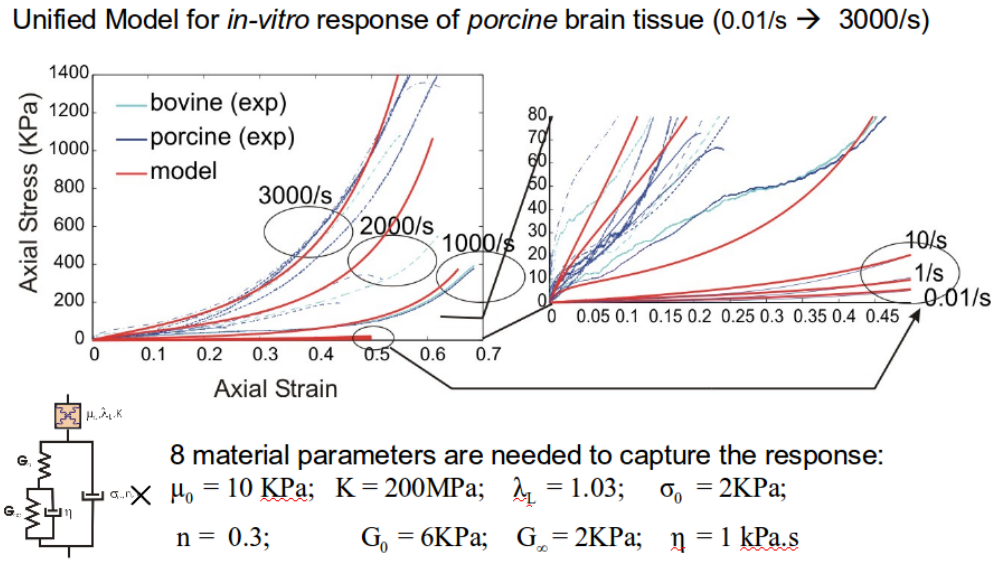

Figure 3: Constitutive modeling of porcine brain in vitro tissue response under a wide range of strain rates. The model captures the response with a single set of parameters

3 Neural-cell shock studies

2011 Project Summary

Professor James Deshler
Department of Biology
Boston University, Boston, MA 02215

I. Research Summary

In this work we sought to determine the cellular mechanisms by which MILD shock waves may damage neuronal cells in the brain. We employed a biolistic gene gun model for shockwave delivery to isolated hippocampal or cortical neurons growing in culture. Using this model we showed that a ~1 psi shockwave transiently permeabilizes the plasma membrane of these cells and reduces the average levels of intracellular ATP. Both membrane permeability and intracellular ATP levels recover by 2 and 24 hours, respectively. However, a longer term affect on these cells is a reduction in synaptic proteins at the post-synaptic site of synapses. In this last year, we showed that pre-synaptic proteins are also diminished at synapses, and we have performed a correlation analysis of triple-labeled blast-exposed cells which indicates that cells with the largest permeabilization have the greatest decrease in synaptic proteins. These data strongly support a causal relationship between membrane permeability and the reduction in synaptic proteins at synapses. While ~1 psi quite mild, a number of recent studies, particularly in rodents, have detected behavioral and cognitive deficits in animals subjected to blastwaves with intracranial pressures in the ~1 psi range. Therefore, we believe that our data provide a potential cellular mechanism by which MILD blastwaves cause neuronal damage that does not involve cell death or axonal injury. This model is now ready for testing in animal models.

II. Recent Results

The concept that shock waves specifically damage synapses before other signs of neuronal damage become apparent in the brain is novel in this field. Interestingly, this phenomenon of "synaptic degeneration first" may be more widespread than investigators have appreciated in the past. For example, it was thought for decades that plaques in the brains of patients with Alzheimer's disease were the primary cause of the cognitive deficits characteristic of this condition. However, the most recent literature in this field involving animal models suggests that the plaques are not the primary etiological cause of AD, but that the cognitive deficiencies characteristic of Alzheimer's patients are actually the result of poorly functioning synapses that have hitherto gone undetected.

During the first and second year of this project, our primary approach involved exposing mammalian neurons to pressure waves and then testing whether or not synaptic degeneration occurs. Cultured rat neurons were exposed to pressure waves of increasing relative intensities using a calibrated biolistic gene gun available in my laboratory. Synaptic degeneration was assessed using quantitative immuno-labeling and fluorescence microscopy of cultured neurons. Using this assay we have shown a statistically significant reduction in the number of synapses per unit length of dendrite on both cortical and hippocampal neurons. These data have been presented at several meetings and seminars. In addition, the data have been submitted, but not yet accepted for publication.

The initial results from the first year of this project combined with our original hypothesis led to a number of further questions that were addressed the second year. We showed that at ~1 psi, no increased cell death was detected in our assay system, but that intracellular ATP levels are reduced up to 50% from 1-24 hours following shockwave exposure. Several mechanisms could account for decreased intracellular ATP observed in cells exposed to mild shock waves. One idea is that membrane channel proteins are partially denatured leading to a selective depolarization of some types of ions across the plasma membrane. This in turn could require a large consumption of ATP to repolarize ions across the membrane. Another mechanism could be the destruction of mitochondria leading to a decrease in ATP production. A third mechanism we considered is that the plasma membrane itself becomes physically damaged and permeabilized from mild shock wave exposure. In this case the damage would be reversible (as is ATP reduction), since it is well known that neurons can recover from such physical damage. To test this last idea, neurons exposed to mild ~1 psi shockwaves and media containing fluorescent dextran and our results clearly showed that these mild shockwaves permeabilize cell membranes. My doctoral student, Matt Ferenc spent a number of months repeating this experiment with different sized dyes and also quantifying the results. The take-home message from all these studies is that the cells do become permeable to relatively small, but not large molecules within 10 minutes of shockwave exposure, and that this permeability is extremely transient such that the membranes are repaired approximately one hour after exposure. *Thus, our **current and refined model** suggests that mild shockwaves transiently permeabilize cells leading to a massive depolarization of the plasma membrane. Since most ion pumps require ATP, intracellular levels of ATP are then depleted not only by diffusion of ATP itself to the cells exterior through the permeabilized plasma membrane, but also through over utilization by enzymes that require ATP to repair cellular damage and restore an electrochemical gradient.* My graduate student Matt Ferenc went on to perform a correlation analysis which shows that cells that take up the most dye in the permeabilization assay have the greatest reduction in synaptic labeling. This work comprises the bulk of Matt Ferenc's thesis, and he recently defended his thesis successfully this summer.

Vanessa Obourne is an MS student in the lab who also finished her thesis at the beginning of summer characterized a number of antibodies to synaptic proteins to determine if any of them become degraded during the time that synapses are degenerating. The reason for doing this is to ***establish a reliable molecular biomarker for detecting shockwave-induced synaptic degeneration in whole animal blast experiments.*** This has been a laborious screen and she has tested over 35 commercially available antibodies. She has shown that some synaptic proteins appear to become redistributed throughout the cell following shockwave exposure, where as a few show a decrease several days after shock wave exposure. These data provided that basis of Vanessa's Master's thesis.

Together, Vanessa and Matt performed similar experiments with dissected rat retinas to determine if the proteins that decreased in cultured neurons exposed to shockwaves displayed a similar response in a complete and normal tissue preparation. Initial results suggest that this is the case giving more credence to the idea that shockwave induced permeabilization leads to reduced levels of synaptic proteins in complex tissues, such as the brain.

III. Significance

Whether or not the approximately 300,000 soldiers returning from Afghanistan and Iraqwith mild TBI actually have physiological damage in their brains that resulted from being in the vicinity of a blast caused by an improvised explosive device is still unresolved. If our hypothesis is correct, the experiments proposed here will provide a conceptual basis with which to understand the cognitive and emotional deficits experienced by at least some individuals exposed to IEDs. Moreover, the technological assays that we develop can then be used to develop drugs and protective materials to help treat and/or prevent cellular and synaptic damage due to blast waves.

IV. Journal Articles

A paper entitled, "A cellular model for mild traumatic brain injury" by Matthew T. Ferenc, Raul Radovitzky, Heng-Ye Man, and James O. Deshler (In Preparation).

Vanessa Obourne, Matthew T. Ferenc, H. Man, and J. Deshler. Identification of synaptic proteins that decrease in response to mild shockwave exposure. (In Preparation).

Matthew Ference and J. Deshler. A method for generating reproducible mild shockwaves using a biolistic gene gun. (To be submitted to the Journal of Visualized Experiments via the request of one of the Journal's editors)

V. Graduate Students Involved Directly in ARO Project

Matthew Ferenc graduated the Ph.D. program this year.

Vanessa Obourne graduated with an MS degree this year.

4 High strain-rate tissue testing

Purdue Contributions to MIT Final Technical Report

Brain Response under Blast and Impact

Wayne Chen and Steve Son
Purdue University, West Lafayette, IN 47907

Abstract

The Purdue tasks of this research project support the MIT/VA blast injury prediction numerical models with accurate experimental data for both initial input and model validation through (i) improving experimental techniques that can accurately determine the dynamic behavior of brain tissues and that can determine pressure distribution and propagation in a simulated brain under blast loading, (ii) determining the dynamic compressive behavior of brain tissues over a wide range of strain rates and stress states, and (iii) recording dynamic pressure propagation and distribution inside a simulated brain with distributed pressure sensors. The Purdue team developed and improved the experimental methods, determined the dynamic compressive behavior of both gray and white matters from brain tissues of bovine, swine, and lamb. We have developed physical models and a systematic approach for testing traumatic brain injury (TBI) mechanisms and occurrences. A simplified series of models consisting of spherical PMMA shells housing synthetic gelatins as brain simulants have been utilized. A series of experiments was conducted to compare the sensitivity of the system response to mechanical properties of the simulants under high strain-rate explosive blasts. Small explosive charges were directed at the models to produce a realistic blast wave in a scaled laboratory setting. Blast profiles were measured and analyzed to compare system response severity. High-speed shadowgraph imaging captured blast wave interaction with the head model while particle tracking captured internal response for displacement and strain correlation. Experiments using both Kolsky bar and DMA have also been conducted on a variety of gels in the effort to find a gel that represents the mechanical response of brain tissues best. Furthermore, a series of open-field and tube-guided blast experiments on simulated brains were conducted with results transferred to MIT. The results suggest amplification of shock waves inside the head near material interfaces due to impedance mismatches. In addition, significant relative displacement was observed between the interacting materials suggesting large strain values of nearly 5%. Further quantitative results were obtained through shadowgraph imaging of the blasts confirming a separation of time scales between blast interaction and bulk movement.

Background

Improved shielding has improved mitigation of shrapnel injuries, however minimizing blast injuries is of increased interest to the Armed Forces. MIT/VA has a current effort in modeling blast loading to the head/neck/shoulder for traumatic brain injury (TBI) predictions [45]. However, realistic predictions from numerical simulations depend critically on the accuracy of the input data on the mechanical response of materials under such blast loading conditions, which is currently scarce. Furthermore, the validation for model predictions also needs experiments conducted under simulated blast conditions. The objective of this work is to provide the data needed to input and validate these models so they can be used in TBI

predictions and then designing improved strategies to mitigate, or at least minimize brain injuries.

There are five major tasks that are carried out at Purdue:

- Design, construct, and improve reliable dynamic characterization tools that can determine the dynamic compressive behavior of brain tissues at high strain rates.
- Conduct dynamic compressive experiments to obtain the dynamic responses of brain tissues and stimulants as a function of strain rate for the purpose of dynamic material model development.
- Transfer results to MIT for material model development as input to simulation codes.
- Design and construct small-scale explosions that simulate large field blast scenarios.
- Conduct explosive driven blast experiments on instrumented head models with stimulant brains for the purpose of numerical model validation.

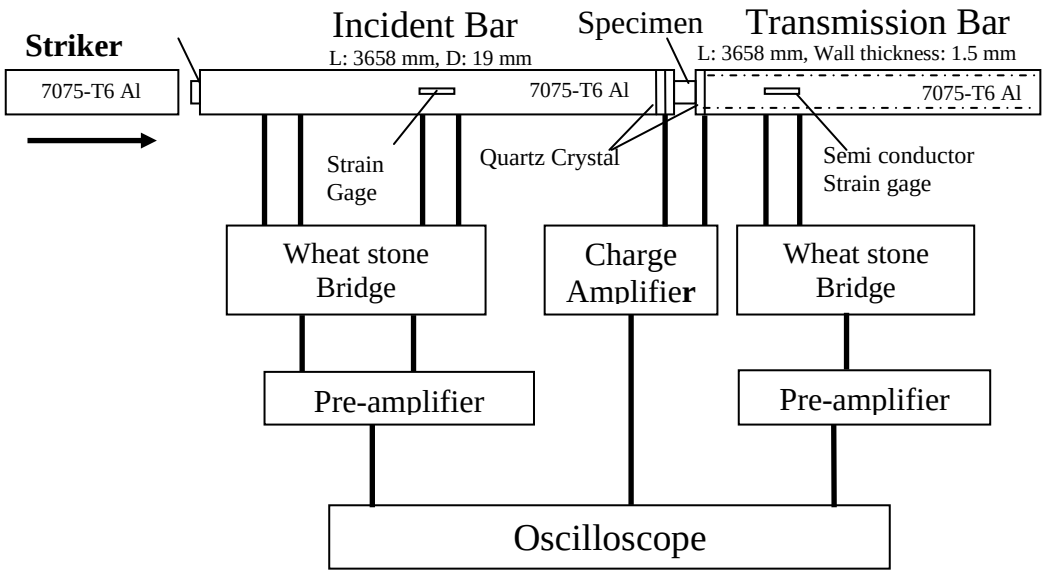

Figure 1: A schematic of modified Kolsky bar for brain tissue characterization

Modified Kolsky Bar for Dynamic Characterization of Brain Tissues

Kolsky bar is a widely used experimental tool for the characterization of dynamic properties of various materials. When brain tissue is under investigation, the low stiffness, low strength and low wave speeds of the tissues poses significant challenges in experiment design for accurate results under valid testing conditions. We modified a Kolsky bar with pulse shaping for uniform loading and constant strain rate, sensitive transmission bar for high-quality load signal, and thin/hollow specimens for inertia effects minimization. The schematic of the modified device is shown in Fig. 1. Three circular piezoelectric transducers were embedded at the end of the incident bar and one was at the beginning of the transmission bar to monitor the time-resolved dynamic equilibrium process. The specimen axial stress was calculated using the semi-conductor strain gage reading from the transmission bar where the stress waves become close to one dimensional.

Dynamic experiments have been performed *in vitro* on brain tissues from bovine, swine, and lamb sources. The brain tissues were collected from a slaughter house in the Animal Science

Department at Purdue University, a few minutes after sacrifice. The tissues were preserved in artificial cerebrospinal fluid at the body temperatures of the animals. All the experiments reported in this paper were completed within eight hours postmortem.

Annulus sample of outer diameter 10 mm, inner diameter 4.7 mm and thickness 1.7 mm were excised from sections of gray matter and white matter. Cylindrical samples were removed with the very sharp edges of a trephine blade, and then the cylinders were sliced to 1.7-mm thick disks by a scalpel with the help of a 1.7-mm thick gage. Finally a 4.7-mm diameter hole was cut through the specimen by a sharp punch, as shown in Fig. 2. The initial sample diameter and thickness were measured with a digital slide caliper. The thin and hollow disc specimen geometry was necessary to minimize both axial and radial inertia effects. Each specimen was prepared just before the mechanical loading.

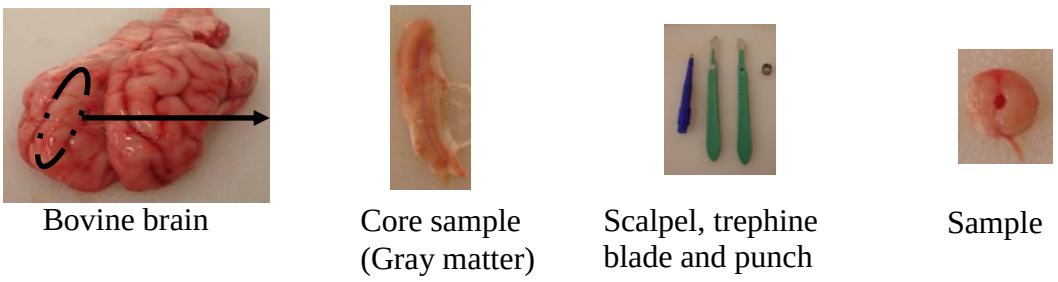

(A) Gray matter

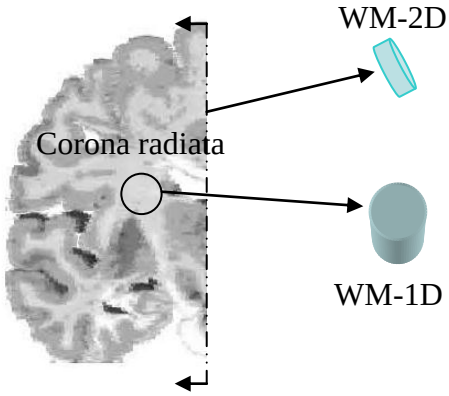

(B) White matter: Sampling directions

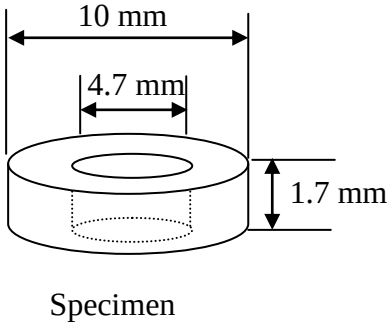

(C) Specimen dimensions

Figure 2: Harvest location for bovine brain samples, indicated by dashed elliptical area for gray matter (A) and farmed circular area for white matter (B) with dimensions (C). Sample preparation from porcine and lamb brain tissues follows a similar procedure.

Dynamic response of bovine brain tissues

In each experiment, the uniform loading and constant strain rate conditions are checked. For each strain rate, fifteen experiments were repeated under the identical testing conditions. The resultant compressive stress-strain curves are shown in Fig. 3 for the gray and white matter from bovine brain tissues. Each of the curves is the average of 15 curves obtained under identical experimental conditions. The stress-strain curves are concave monotonically upward for all strain-rates until unloading. The tissue response stiffened with increasing rates even within the quasi-static range, which is consistent with the results reported at lower strain rates up to 0.64 s^{-1} in the literature [46].

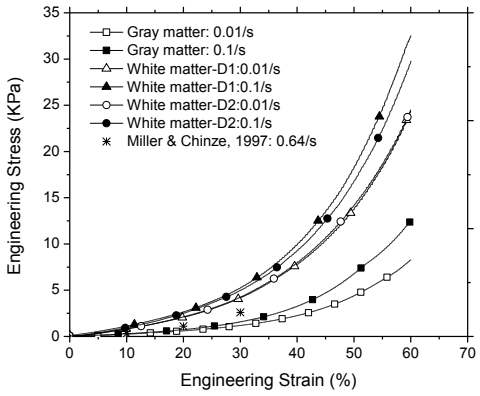

(A)

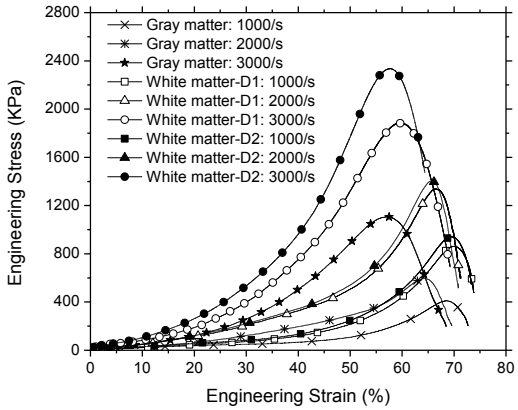

(B)

Figure 3: Compressive stress-strain curve of bovine brain tissues at quasi-static (A) and dynamic (B) strain rates. Each curve is the average of 15 identical experiments.

Dynamic response of porcine brain tissues

Similar experiments are conducted on specimens obtained from porcine brain tissues. The resultant stress-strain curves are shown in Fig. 4 for gray matter and Fig. 5 for white matter.

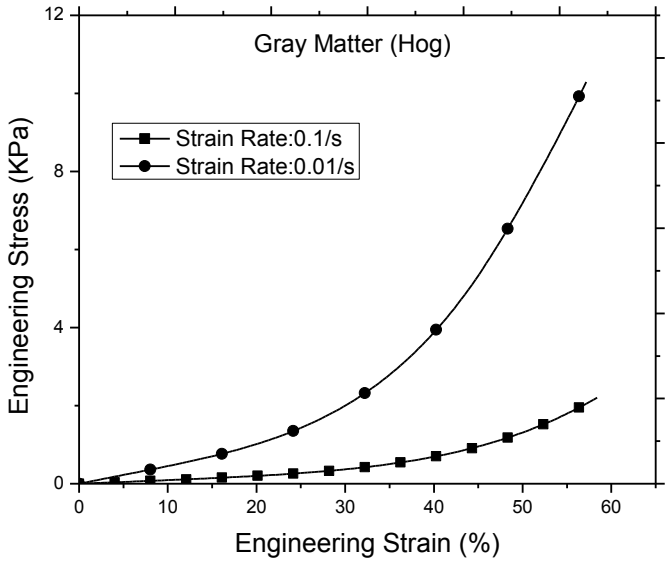

(A)

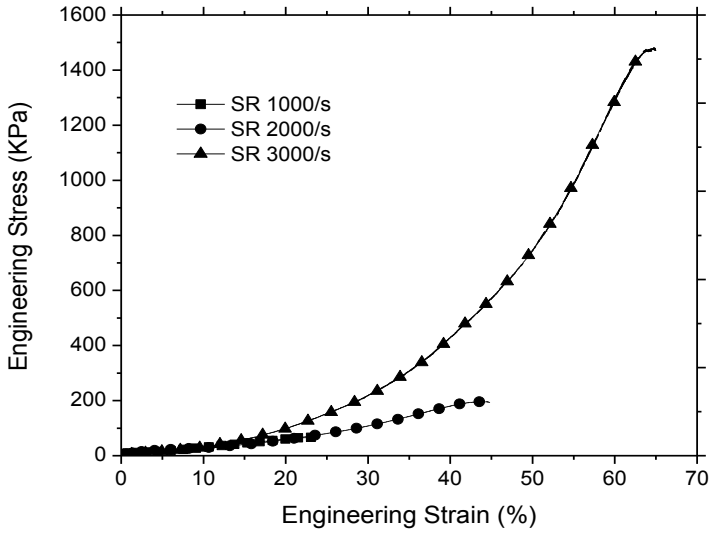

(B)

Figure 4: Compressive stress-strain curve of gray matter of porcine brain tissues at quasi-static (A) and dynamic (B) strain rates.

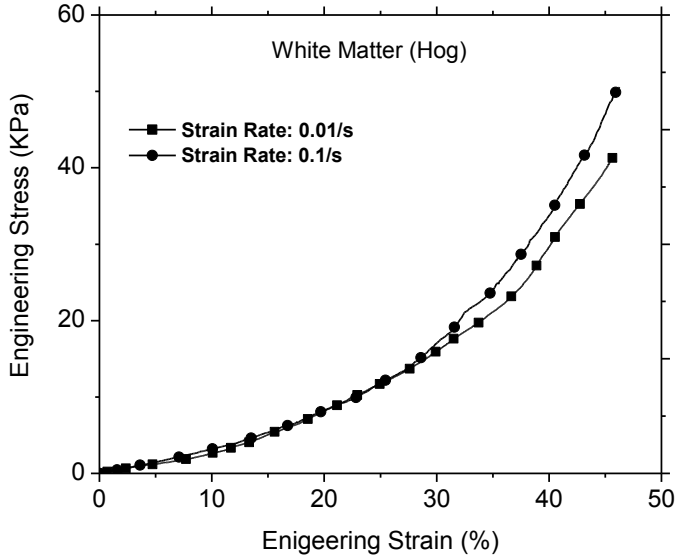

(A)

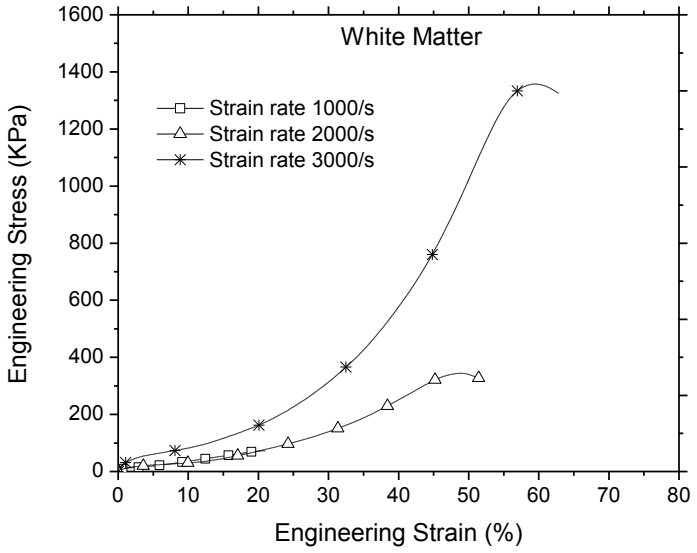

(B)

Figure 5: Compressive stress-strain curve of white matter of porcine brain tissues at quasi-static (A) and dynamic (B) strain rates.

Dynamic response of lamb brain tissues

Similar experiments are conducted on specimens obtained from lamb brain tissues. Due to specimen size limitations, experiments were conducted only on gray matter. The resultant stress-strain curves are shown in Fig. 6.

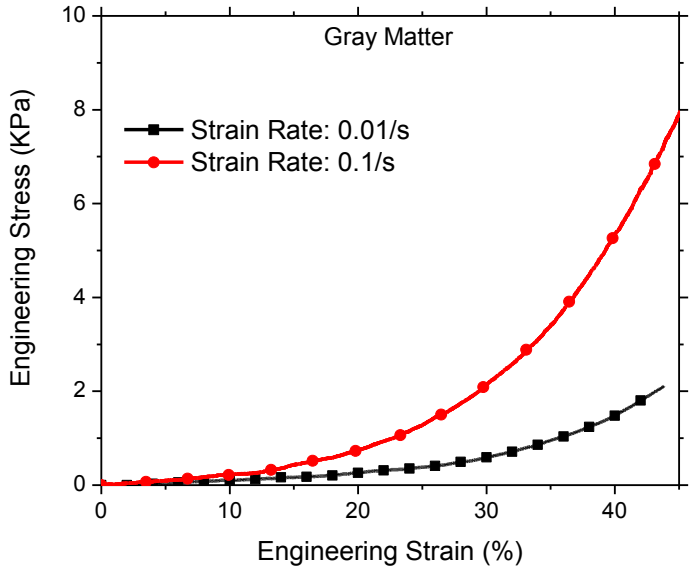

(A)

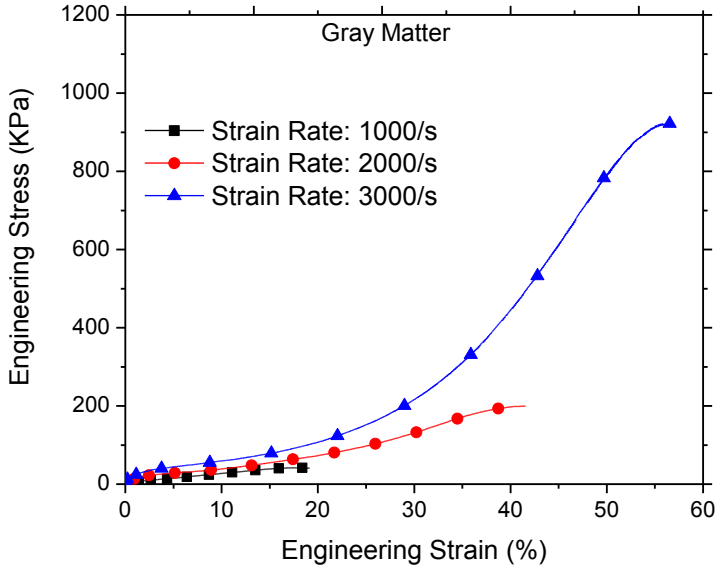

(B)

Figure 6: Compressive stress-strain curve of gray matter of lamb brain tissues at quasi-static (A) and dynamic (B) strain rates.

Comparison of dynamic response of brain tissues from different animals

Figure 7 shows the compressive stress-strain response of gray matter of bovine, hog and lamb brain tissues at the strain rate of 1000/s. The results indicate that there are no significant inter-species variations among the steer, hog and lamb brains at this strain rate. The results from a wider strain rate range from 0.01 to 3000/s show similar trend [48]. The differences between the stress-strain curves from brains of different species are within the error bands from the results on one specific brain [47].

To compare the possible gender differences, we conducted compression experiments on brains from male and female cross-bred pigs at the strain rate of 1000/s. Figure 8 shows the resultant stress-strain curves, which indicate that the brain tissue has no gender difference in terms of mechanical properties when compressed at the high strain rate. To determine the differences between different types of pigs, dynamic compression experiments were performed on the brain tissues harvested from 6-month old pure bred and cross bred Yorkshire gilts. Figure 10 shows the compressive stress-strain curves obtained at the strain rate of 3000/s, where no apparent differences can be observed.

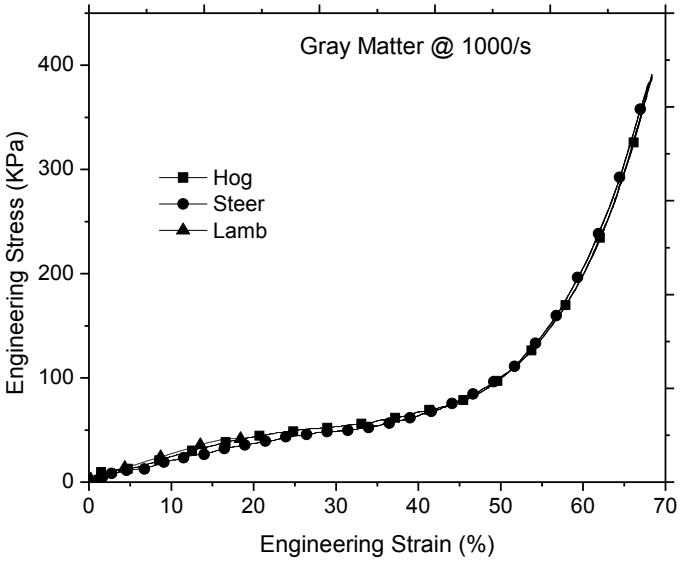

Fig. 7: Compressive stress-strain response of gray matter of bovine, hog and lamb brain tissues at strain rate of 1000/s.

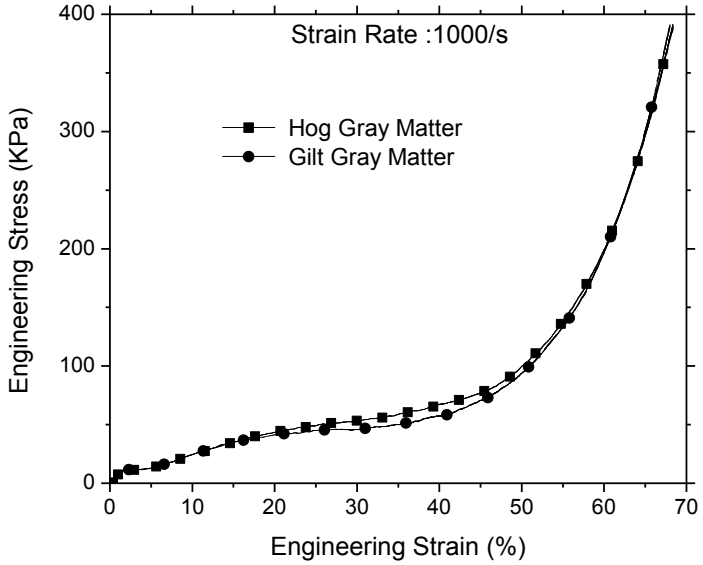

Fig.8. Comparison of the male and female hog brain tissues at strain rate of 1000/s

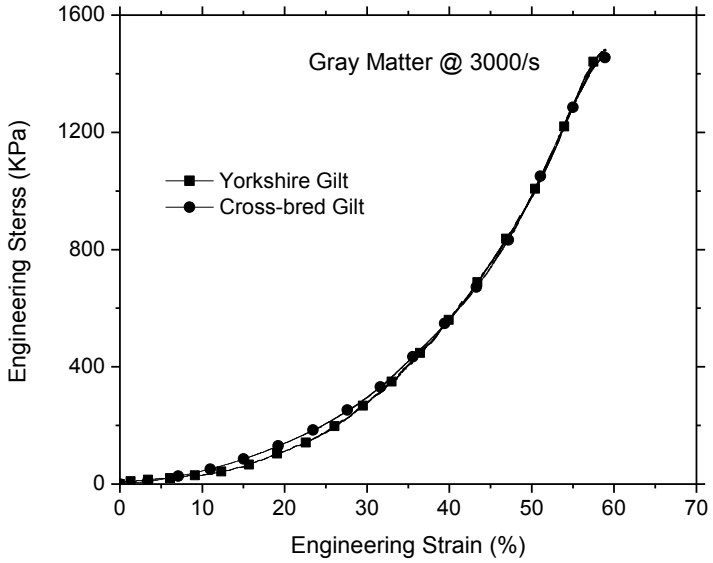

Fig.9. Comparison of the pure bred and cross bred Yorkshire gilt brain tissues at 3000/s

Dynamic response of gels and brain tissues from Kolsky bar and DMA experiments

Similar Kolaky bar (SHPB) experiments are conducted on specimens from gel materials that are intended to be used as brain tissue stimulants. Figure 10 shows the comparison of the compressive stress-strain behavior of selected gels and the bovine brain tissue under both quasi-static and dynamic loading conditions.

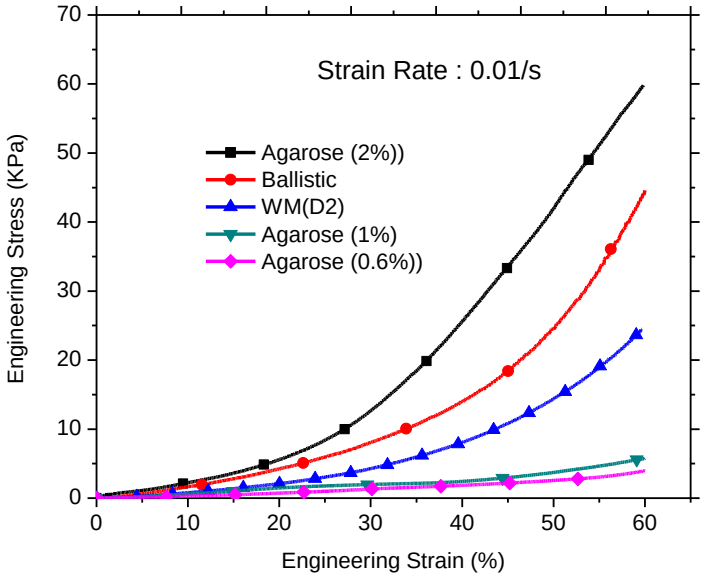

(A)

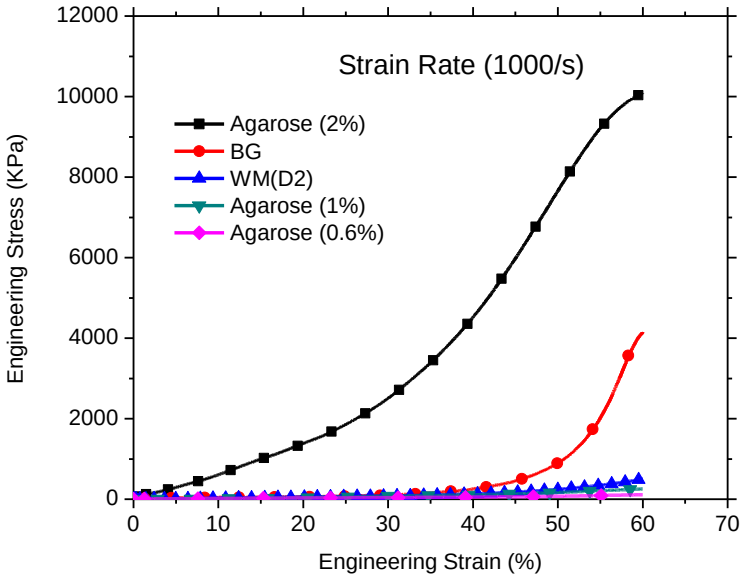

(B)

Figure 10: Compressive stress-strain curve of selected gels and bovine white matter at quasi-static (A) and dynamic (B) strain rates.

The results in Fig. 10 hits that the compressive mechanical response of the bovine white matter is close to the response of the Agarose gel at the concentration of about 1%. We further compared the high-rate mechanical responses of Agarose 1% gel and brain tissue at small strains using a dynamic material analyzer (DMA). The results, as shown in Fig. 11, indicate that the 1% Agarose gel is still stiffer than the brain tissue. The experiments are being continued in an effort to find a brain tissue stimulant that represent the dynamic response of brain tissues.

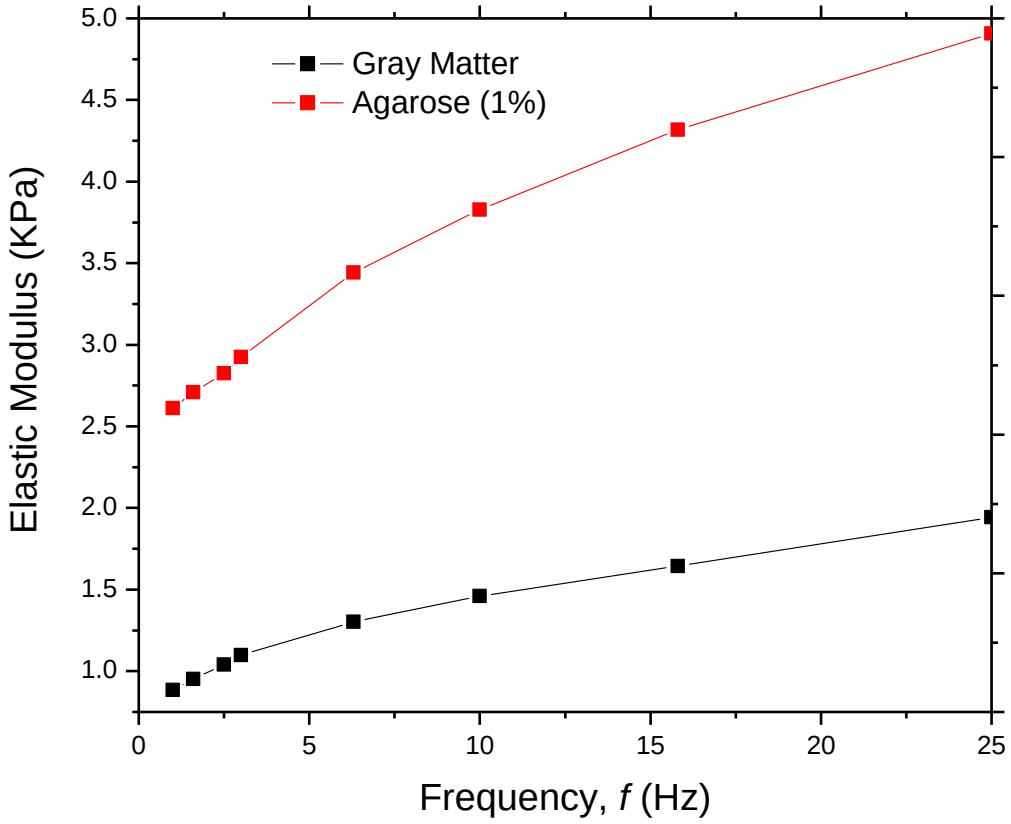

Figure 11: Comparison of the response of 1% Agarose gel and bovine gray matter from DMA.

Laboratory-scale blast loading experiments

Although secondary, tertiary, and quaternary injuries all occur in the field, primary blast injury is the specific injury of interest within this study. It was therefore assumed that primary injuries were the limiting factor in order to characterize system response at and below primary

blast injury fatality levels. The data presented in Table 1 is a summary of approximate blast damage levels presented by Kinney and Graham. in table XV of [29].

Table 1. Blast damage – overpressure correlation [29].

Type of Damage	Overpressure (psig)
Personnel knocked down	~ 1 - 1.5
Eardrum rupture	~ 5 - 15
Lung damage	~ 29 - 75
Lethality	~ 100 - 220

Additionally, Cooper [30] and Bowen [31] present air blast fatality curves for a 70 kg man standing in the path of a blast and facing any direction relative to the blast [30,31]. Comparing the approximate blast damage levels in Table 1 for fatality with the probability of fatality from the air blats fatality curves supports an estimate of 1% probability of fatality at 100 psig and 90% probability of fatality at 220 psig. Therefore, it was determined that levels below 100 psig would be sufficient for laboratory testing to characterize system response to a loading condition in the field producing injury but not necessarily fatal injury.

After specifying the overpressure range of interest, necessary standoff distances were determined. As the focus of this study was small-scale laboratory testing methods for TBI occurrences, small three gram charges of pentaerythritol tetranitrate (PETN) plastic sheet explosive were chosen for the experiments providing an explosive yield of 13.24 kJ and TNT (trinitrotoluene) equivalent mass of 2.872 grams. The PETN plastic sheet explosive consisted of 63% PETN powder, 29% plasticizer, and 8% nitrocellulose with a density of 1.48 g-cm^{-3} and detonation velocity of 6.8 km-s^{-1}. Initiation of the PETN was produced by a length of 50 grain detonation cord (PETN powder) that was connected to a Teledyne RISI RP-502 explosive bridgewire detonator charged by a Teledyne RISI FS-62B firing set. Following the scaling prediction procedure described in [29] and the characteristics of the PETN datasheet, blast profile predictions were determined and standoff distances were defined. The predicted profile characteristics as determined from the scaling correlation prediction methods of Kinney and Graham [29] are shown in Table 2.

Table 2. Scaling predictions for laboratory blast parameters.

Standoff Distance	Overpressure [psig]	Positive Pulse Duration [ms]	Impulse (I/A) [psig-ms]
8 inches (0.2032 m)	66	0.12	2.18
12 inches (0.3048 m)	26	0.18	1.72
16 inches (0.4064 m)	13	0.23	1.37
17 inches (0.4318 m)	12	0.24	1.3

The interaction of the blast wave was introduced by means of a uniquely designed explosive-driven shock tube (see Figure 12) in order to direct the blast energy toward the target. The shock tube design consisted of a 12 inch detonator chamber capped at one end and a 36 inch high explosive (HE) chamber also capped at one end. The capped ends were bolted together once the

chambers were loaded for firing. The detonator chamber prevents fragmentation from the aluminum detonator cap into the room and target as the focus of these studies was on the blast itself and not fragmentation of any kind. The long HE chamber provided extra distance for shock wave/product separation, as well as minimizing reflections and turbulence at the exit. Shock waves fundamentally occur only in supersonic conditions whereas the detonation products travel approximately at local sonic speeds. Therefore, the additional length of the HE chamber provided greater separation between shocks and fireball for imaging purposes, as well as greater time to smooth the blast wave compared to the blasts of open air charges closer to the targets.

High-speed shadowgraph imaging was performed for visualization of the experimental blast waves according to methods developed by G. Settles at The Pennsylvania State University[32]. The shadowgraph imaging provided a qualitative representation of the shock wave interaction with the various models being studied. Furthermore, the shadowgraph images could be analysed quantitatively using tracking features of the imaging software to provide data regarding the shock wave position with time. A Vision Research Phantom v7.3 digital high-speed camera was used to record the blast phenomena, typically at a frame rate of 36,036 fps and a resolution of 256 x 256. Using a 45° turning mirror affixed to a UV filter on a Sigma 24-70mmD f/2.8 EX DG Aspherical lens, a high intensity light beam was directed across the model onto a reflective screen via a Oriel 1000 W xenon arc lamp [32]. The shadow of the model and shock wave interaction were then recorded as density changes were experienced causing changes in the refractive index [33]. Figure 13 diagrams the experimental setup.

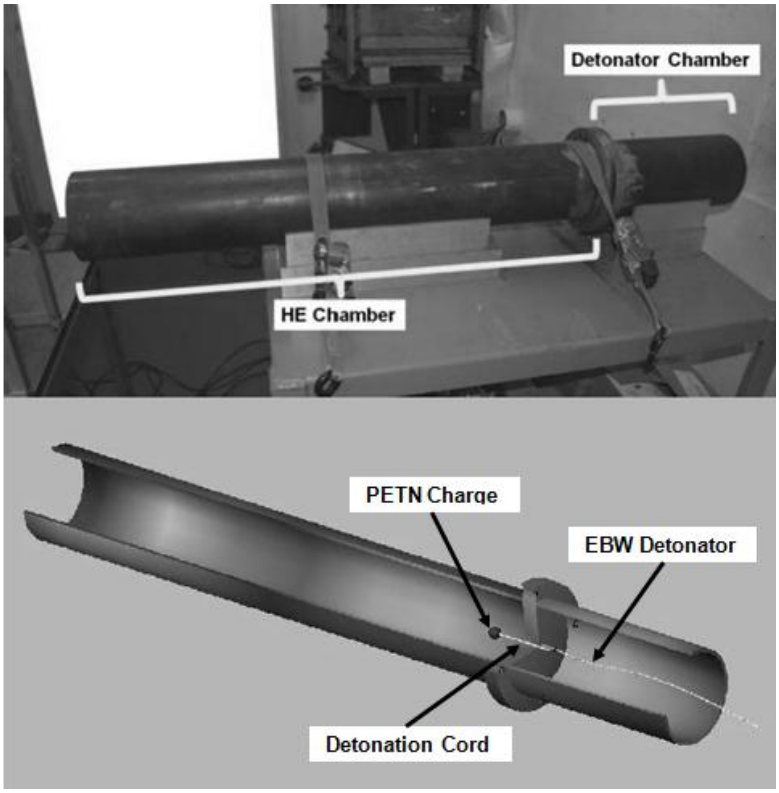

Figure 12. Explosive driven shock tube.

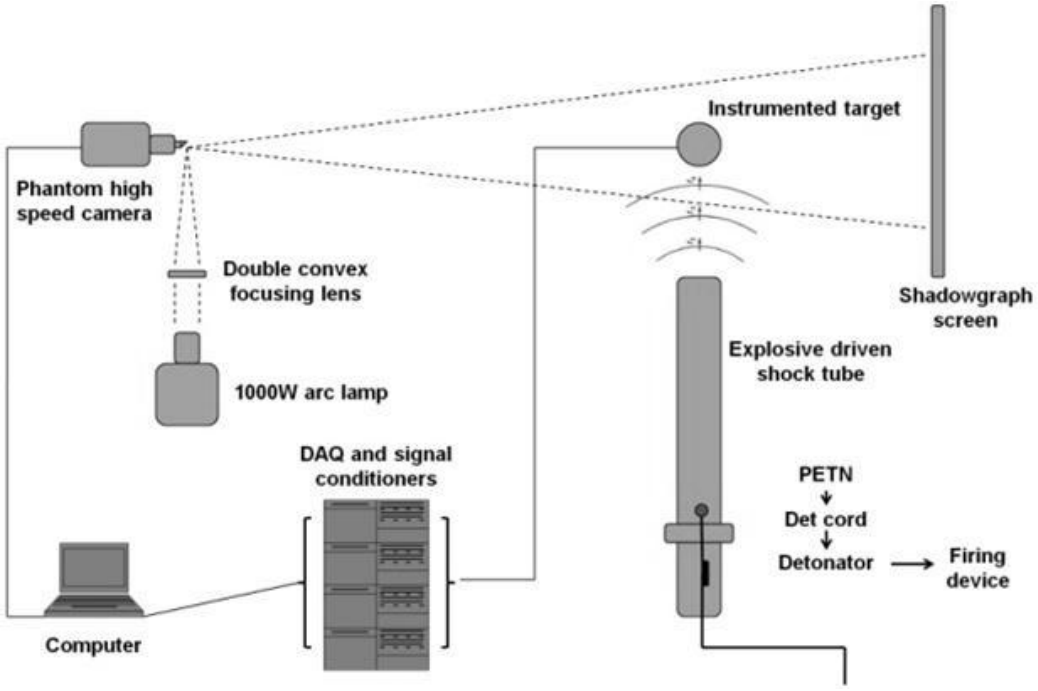

Figure 13. Experimental setup.

Utilizing the shadowgraph imaging, it was possible to test and record the performance of the PETN sheet explosive with the explosive driven shock tube. A series of experiments were performed without targets in place and imaged to record shock parameters as a function of time. Using the point tracking feature of the Phantom 649 control software, the shock distance was measured with time. The distance-time data was then curve fit and differentiated to develop a predicted wave speed function. Using the curve fit wave speed function, expected shock pressures were calculated according to pressure ratio equations from the normal shock relations of compressible flow dynamics. The performance of the explosive-driven shock tube as derived from the shadowgraph imaging is summarized in the speed-distance profile (see Figure 14) and the pressure-distance profile (see Figure 15). Contained in the pressure plot are the predicted overpressure values derived from the scaling correlations of Kinney and Graham [29] for the four standard loading conditions to be used in this experimentation. All but the nearest standoff distance compare well with the measurements. This deviation may have been expected due to the scaling correlations idealized assumptions breaking down close to the charge. In addition to the imaging-derived performance, the actual pressure profiles were measured to characterize the four standard loading conditions. Figure 16 shows the results of these measurements for the standard loading conditions applied to the model systems. The blasts were measured using PCB model 137A24 free field blast pressure pencil probes. The gauge measurements then were conditioned and amplified using PCB model 482A22 signal conditioners and the data was recorded using Tektronix DPO4034 oscilloscopes. The results of these standard loading profiles showed blasts with overpressure values in fair agreement with the imaging-derived pressure values and with the scaling correlation predictions, although the gauge-measured value exceeded the predictions at the closest standoff distance. Furthermore, the actual duration and impulse of each of these measured laboratory blasts exceeded the predicted values by an average of four and one half times and four times, respectively. Therefore, these results suggest that by using the explosive-driven shock tube, the energy of the blast is directed towards the target and enhanced

to simulate a larger IED blast than would be possible with the same charge in open air. Specifically, the measured blast parameters (overpressure and width) correspond closely to charges of 200 grams to 300 grams at standoff distances of 30 inches to 70 inches (0.76 m to 1.78 m) which closely resemble hand grenade size IED sources. Additionally, further shock tube work could be performed with a longer tube geometry that would better replicate even larger explosive charge blasts. Charge sizes could also be increased as well.

Finally, in order to validate the blast measurements being made, 12 experiments were performed without targets in place again to compare the repeatability of the small-scale blasts. The blasts were measured at a standoff distance of 12 inches (0.3048 m) using both PCB model 137A24 free field blast pressure pencil probes and PCB model 113B22 pressure sensors for comparison. The results of the 12 experiments resulted in standard deviations of 10% for impulse, less than 5% for arrival time and duration, and 15% for peak overpressure suggesting acceptable overall repeatability in the method.

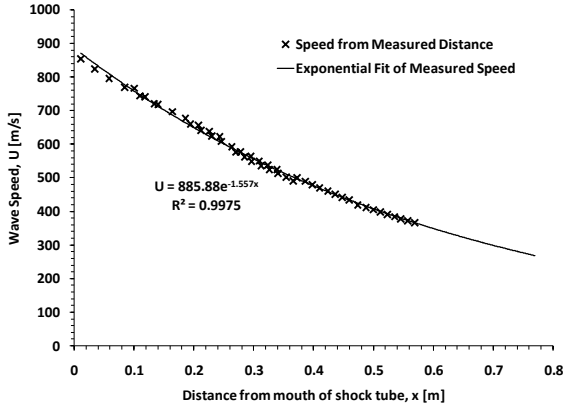

Figure 14. Wave speed from measured x-t shock position of explosive driven shock tube.

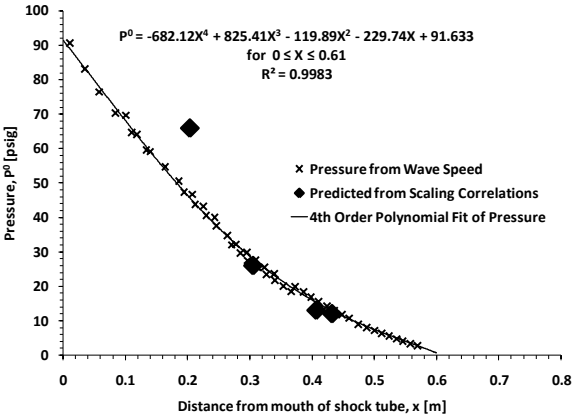

Figure 15. Pressure derived from measured x-t shock position.

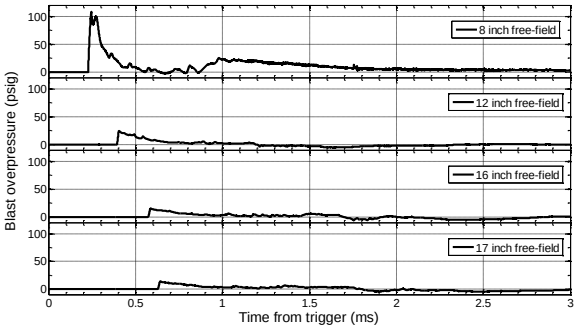

Figure 16. Standard experimental loading conditions

Surrogate model series

The approach taken was to simplify the anatomy of the human head into surrogate laboratory models. As the nature of shock waves is complex to begin with, the interaction of shock waves with obstacles becomes even more complicated. Therefore, it was necessary to initially produce lower fidelity physical models and then later gradually introduce the complexities of geometry and material variations involved with shock wave/obstacle interaction. This effectively provides a basic starting point for experimental validation and comparison of computational simulations and clinical observations.

The progression of experimental fidelity included six model systems to accommodate the varied combinations of geometry and material selection (see Table 3).

Table 3. Experimental model progression.

Model	Shell Geometry	Tissue Geometry
A	PMMA solid	Perma-Gel™ hemispheres
B	PMMA cutout	Perma-Gel™ hemispheres
C	PMMA solid	Perma-Gel™ sphere
D	PMMA cutout	Perma-Gel™ sphere
E	PMMA solid	PDMS sphere
F	PMMA cutout	PDMS sphere

Models A – F utilized two clear, injection-molded PMMA hemispheres of dimensions: 5 inch outer diameter and 0.125 inch wall thickness. The hemispheres were bonded together with plastic weld to form the full sphere model, encompassing a volume of ~56.12 in^3. Each sphere was then fitted with hardware to be supported in a non-rigid, pendulum method from the test stand. The PMMA shell was varied between a solid shell and a shell with rough facial features (eyes, nose, and mouth) manufactured in the anterior surface. The selected features included two 0.75 inch circular cutouts representing eye sockets, one 0.5 inch circular cutout representing the nasal passage, and one 0.75 inch circular cutout representing the mouth (see Figure 17). The purpose of the facial features was to compare the difference in the internal system response from the solid shell models. This comparison was made in response to the suggestion from the literature that suggested ocular/nasal/aural pathways as mechanisms of blast wave entry into the cranial cavity [10].

The model shells were then filled with one of the two brain simulants: Perma-Gel™ ballistic gelatin and polydimethylsiloxane polymer (PDMS). The two brain simulants represent two

extremes. The Perma-Gel™ provided a low strain-rate dependent material with significant deviations from biological properties but simpler to computationally model. The PDMS provided a more rate dependent material with properties more closely representing biological samples (very similar texture/consistency to brain matter when physically touched) but also more complex to model.

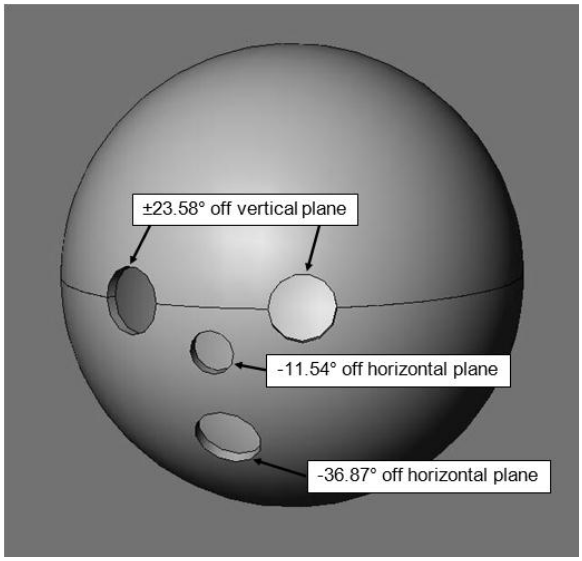

Figure 17. PMMA shell with facial feature cutouts.

In reference to all materials used, the complexity of the human anatomy, manufacturing limitations, and analysis capability prohibits exactly matching surrogate material properties to true biological material properties. Rather, the values of the materials were determined, with acknowledgement of the differences between surrogate and biological. The materials used in the experimental procedures provided a range of mechanical properties as a means of studying the effects of those property variations on shock wave interaction. The variations also provided a method to determine the ability to experimentally distinguish possible injury phenomenon using higher or lower fidelity materials. The accepted biological values determined by the project collaborators [34] are compared with the surrogate material properties in Table 4. Although single property values (rather than ranges of values) have been identified for each biological specimen, the referenced literature for these properties provides ranges of accepted values bracketing those listed in the table. The listed values represent typical values for better clarity.

Table 4. Mechanical properties [35-40].

Brain	ρ [g/cm^3]	ν	E [kPa]	c [m/s]	Z [kg/m^2-s]
White matter [35, 36]	1.06	0.5	37	6	6,360
Grey Matter [35, 36]	1.06	0.5	30	5	5,300
Perma-Gel™ [37, 38]	0.89	-	Order of ~100	10	8,900
PDMS [38]	0.92	0.5	Order of ~4.5	2	1,840

Skull	ρ [g/cm^3]	ν	E [GPa]	c [m/s]	Z [kg/m^2-s]
Bone [36, 39]	1.41	0.22	6.65	2170	3,059,700
PMMA [40]	1.19	0.37	3	1590	1,892,100

The models were instrumented in order to capture internal system reaction resulting from the shock wave interaction with the interference. Initially, miniature fiber optic pressure sensors from FISO Technologies, which were minimally invasive, were tested in the models. However, several problems were observed early on with the sensors. Dynamic performance specifications

for the sensors were unavailable, therefore, making it impossible to determine if the sensors could respond appropriately to the rapid time scales of interest. Furthermore, eratic behaviour from the sensors was observed such as minimal to no response and DC shifts in the output data. Therefore, PCB Piezotronics dynamic pressure sensors were used due to the available specifications and stable behaviour. Models A – F were instrumented as follows. PCB model 113A22 and 113B22 dynamic pressure sensors were embedded (vertically centered) within the tissue simulants at distinct locations for shock wave characterization. Each model utilized three sensors at an anterior, lateral mid-plane, and posterior location. A single PCB model 352A25 accelerometer was externally affixed (vertically centered) to the outer posterior surface of the shell. The exact positions of each gauge are represented in Figure 18. The data was conditioned and recorded using PCB model 482A22 signal conditioners and Tektronix DPO4034 oscilloscopes respectively. Upon collection of the data, all datasets were then digitally filtered through a 100 kHz low-pass filter to reduce noise and signal interference prior to analyzing.

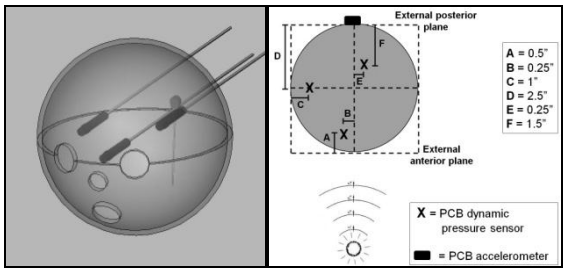

Figure 18. Sensor placement for models A - F.

Many injury theories involve pressurization of the tissues in the cranial cavity, access of the blast wave into the cranial cavity, and coup-contrecoup injuries resulting from accelerations [10-14]. The use of the applied instrumentation described previously was intended to provide some insight into these damaging aspects of the explosive driven shock waves. However, the data from the instrumented models should not be considered exhaustive. In addition to the injury mechanisms mentioned, it has also been suggested that the application of the blast wave could cause shearing of tissue, vascular regions, and axons [3,11,17,18]. The application of an external force, such as the blast pressure, results in stress and deformation of the material. With severe enough pressure profiles, material limits can be exceeded and therefore disrupt specific brain features that could lead to cognitive deficits and various other symptoms. Therefore, in order to study these effects, two additional models were utilized. These models consisted of 1 inch wide PMMA rings of outer diameter 5 inches and wall thickness of 0.125 inches. The discs represented slices of the overall spherical PMMA shell models in order to reduce the geometry to a 2D configuration. The discs were then cast with the Perma-Gel^{TM} ballistic gelatin and sandwiched between two additional pieces of PMMA of thickness 0.125 inches. During the casting process, a centre plane was established at 0.5 inches from either face on which a speckle pattern was painted on a single face. The pattern was applied by means of spray can application in order to distribute 1-3 mm non-uniform speckles across the face. The purpose of the speckle pattern was to allow for imaging of the internal motion in response to the blast input. The frame by frame image sequence was then input into a correlation software package, Vic-2D, published by Correlated Solutions, Inc. Vic-2D utilized white-light speckle correlation to provide displacement and strain fields for objects over a wide range of sizes experiencing a wide range of strain values [42-44]. The limitations of the Vic-2D analysis required motion to be restricted to two dimensions and therefore out of plane motion had to be minimized as much as possible for

best accuracy. As a result, the strain mapping procedures were limited to the 2D disc configurations and were not applied to the spherical shells in their entirety.

Results

Figures 19-21 show the averaged results of the internally recorded pressure measurements for the various standoff distances, geometric configurations, and gelatin materials. Each model was subjected to two repetitions of loading at each standoff distance. The comparison between repetitions showed close agreement for each model. These sets of repetitions were then compiled to produce average trends shown the results summary figures. Refer to Figure 22 for a typical plot of the internal pressure profiles. Several general trends can be seen between all models. According to the standoff distances of the models, the measured loading conditions applied (free-field blasts) ranged from approximately 15 psig to 108 psig. The recorded pressures at the anterior gauge location for each model showed significant pressure amplification (pressures around 300 psig to 500 psig). The pressure amplification might be expected, however, when considering the impedance mismatch between air, PMMA (bone), and gelatin (brain matter). While air has an impedance of approximately Z = 420 kg/m^2-s, both gelatins have an impedance roughly an order of magnitude larger than air and PMMA and bone have impedances nearly four orders of magnitude larger than air. With the large impedance mismatches present at the boundaries, one would anticipate a significant pressure rise across the interface due to standard shock propagation behaviour. Furthermore, the pressure enhancement at the anterior location might also be caused by the geometric focusing of the shock waves as a result of the curved surface of the shell. The shape potentially causes directed reflections resulting in wave interaction and convergence that might add to the pressure amplification. This recorded phenomenon also coincides with results of computational work presented by Taylor et al. [12] suggesting focused pressures at or near interfaces as well as computational results of Prof. R. Radovitzky and team at the Massachusetts Institute of Technology [34]. A comparison of the peak overpressures across all locations shows that the PDMS polymer generally sustained lower peak pressures at the anterior gauge location than the Perma-Gel^{TM}, as would be expected due to the lower impedance of the PDMS polymer. However, at the mid-plane and posterior gauge locations, the PDMS peak pressure values began to exceed those of the Perma-Gel^{TM}. Additionally, the PDMS polymer generally sustained longer pulse durations than the Perma-Gel^{TM}. The long durations coupled with larger pressures lead to larger impulses experienced in the PDMS. The larger impulses then suggest a more severe response to the blast than that of the Perma-Gel^{TM}, suggesting a higher probability for injury. These data provide critically needed validation for computational models. Comparisons with computational models will be presented in future papers.

Additionally, the effects of the material variation coupled with the geometric variation of the facial features can be seen by significant variations in response when comparing results of the two gelatins. As stated before, the PDMS polymer generally responded with more severe impulses and durations but lower pressures than the Perma-Gel^{TM}. Once again, the impedance of the PDMS polymer is greater than air but not near as large as that of Perma-Gel^{TM}, which would suggest less initial amplification but greater overall transmission through the model. An additional characteristic of the material variation was the apparent stochastic behaviour of the

Perma-Gel™. While the PDMS polymer generally showed smoother, consistent trends, the Perma-Gel™ tended to exhibit more stochastic features.

When comparing the effects of the facial feature cutouts, the PDMS polymer showed significantly greater variation between solid shell responses and cutout shell responses than did the Perma-Gel™ models. At anterior locations, ocular/nasal effects were minimal as the response amplification was already severe regardless of the model or standoff. However, at the mid-plane and posterior locations, the PDMS models generally responded with approximately 30% - 50% variation between solid shell models and facial feature models for pressure and above 50% variation for impulse between solid and cutout shells. Specifically, impulse values were 50% higher in the facial feature models than the solid shell models. Alternatively, the Perma-Gel™ response variations were generally much less than those of the PDMS. Furthermore, the effect of casting the simulant as hemispheres versus spheres was seen in response variations from the solid shell and cutout shell models. With the hemispherical casts, the responses generally were very similar between solid and cutout shells. Less severe blast characteristics were typically experienced as well. The result of casting the simulant as a solid sphere seemed to suggest better continuity in the system as well as eliminating additional stochastic behaviour in an already complex and randomly behaving material.

The acceleration measurements obtained at the posterior surface of the shell revealed extreme accelerations experienced by the model. Magnitudes of up to 6000 g's were experienced according to standoff distance. High frequency oscillatory behaviour was evidenced from the acceleration traces revealing a peak magnitude initially experienced when the shock first contacted the model on the anterior side. The acceleration was then quickly damped out within the same time scale (~5 ms) as the occurrences of the internal measurements. The general trends between each model were similar and showed less distinguishing characteristics. However, it is important to note that in general the models experienced extreme acceleration forces momentarily. Furthermore, the shock interaction with the gauge may affect its reading and may not reflect a true acceleration, at least for early times. Refer to Figure 23 for a representative acceleration trace.

In addition to the temporal data, the model datasets were contrasted by their power spectral density (PSD) profiles. The calculated PSD profiles are a frequency decomposition of the pressure signals in order to distinguish the power at specific frequencies. As they must, the general trends agree with those seen in the time domain and therefore provide just another tool to analyse the data. The anterior profiles typically showed higher power magnitude for a wider range of frequencies, corresponding to large, sharp features in the time domain. Furthermore, the PDMS models generally had moderately higher magnitudes than the Perma-Gel™ models over a wide range of frequencies as well. The Perma-Gel™ models typically showed a steeper roll off than the PDMS models. As the Perma-Gel™ models typically began to decay around 1 kHz – 2 kHz, the PDMS models tended to hold steady until around 10 kHz or greater. Even then, the more severe standoff distances showed higher power magnitudes remaining steady across the entire frequency band for the PDMS models. At the closer standoff distances, the distinctions between materials became more evident while the trials at the farther standoff distances showed less variations between models. See Figure 24 for a typical PSD profile.

Beyond the internally recorded gauge measurements, an important characteristic was determined from the shadowgraph imaging. According to multiple shadowgraph videos of the various models, noticeable global target movement was not recorded until after approximately 3 ms to 4 ms. Initial shock loading was experienced by the model for approximately 0.25 ms after

arrival times ranging from approximately 0.14 ms to 0.5 ms depending on standoff distance. Over an average video duration of 9 ms, less than 5 degrees of angular rotation were experienced by the model. This result suggests and confirms the importance of two overall time scales where primary injury can potentially occur before secondary and tertiary effects take place. Specifically, the large anterior pressure spikes occurred before significant bulk motion. These are large enough to anticipate biological damage. Impacts would not be expected to result in similar behavior. In addition to the global movement feature shown in the shadowgraph images, one can see the effect of shock wave interaction with varying boundaries. Once again, the impedance mismatch is a key factor in the interaction. The physical phenomenon of the mismatch is represented in the sequential shadowgraph frames of Figure 25 representing a typical experiment.

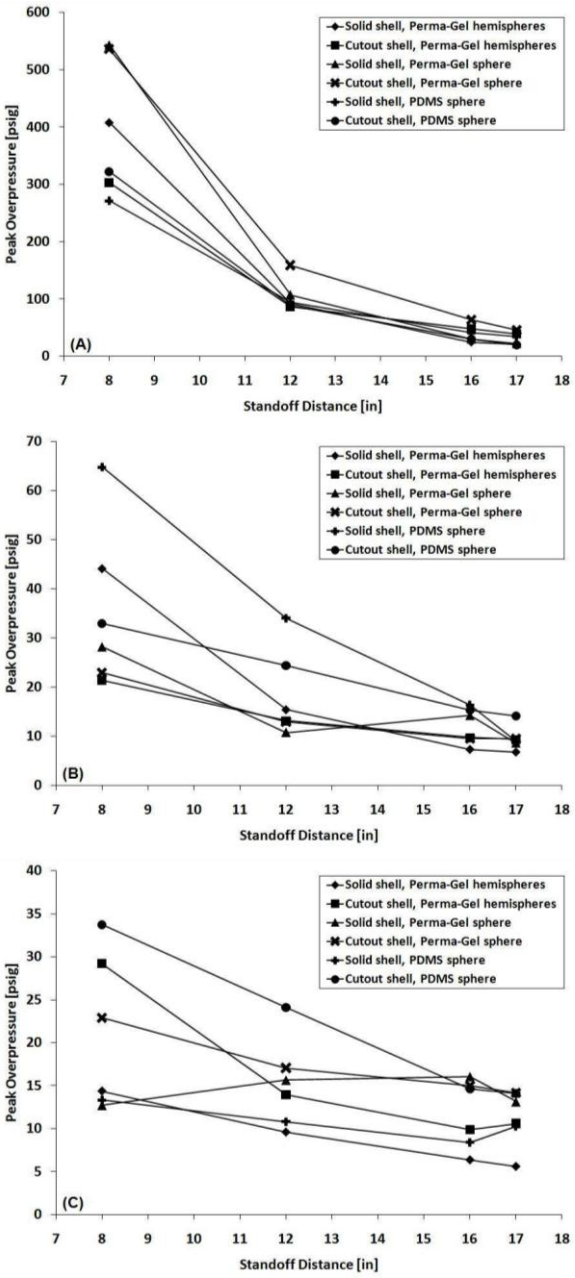

Figure 19. Peak overpressure results for anterior (A), mid-plane (B), and posterior (C) gauge.

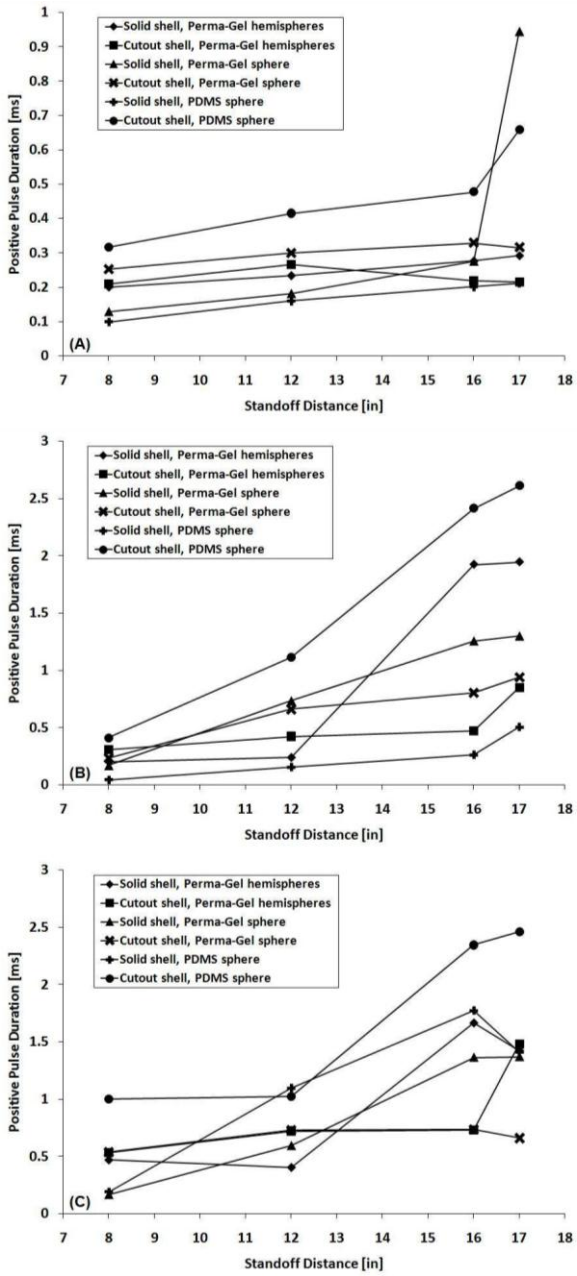

Figure 20. Positive pulse duration results for anterior (A), mid-plane (B), and posterior (C) gauge.

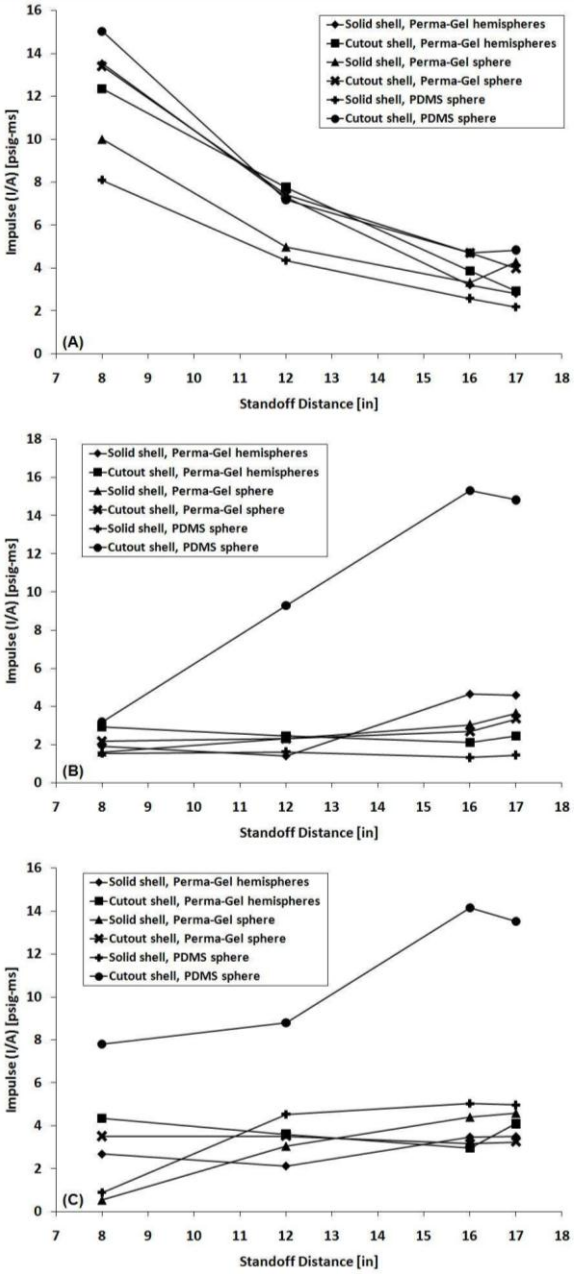

Figure 21. Impulse results for anterior (A), mid-plane (B), and posterior (C) gauge.

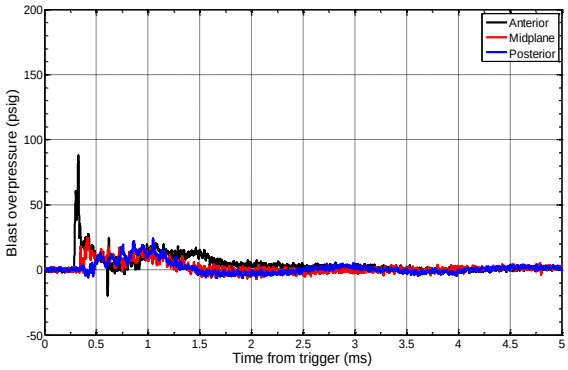

Figure 22. Representative internal pressure experienced by spherical PMMA shell surrogate head models (model F result shown at 12 inch standoff).

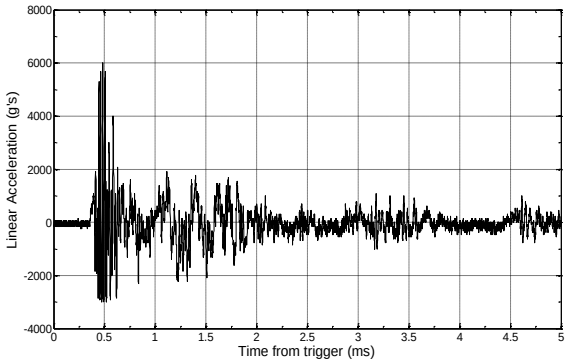

Figure 23. Representative linear acceleration experienced by spherical PMMA shell surrogate head models (model F result shown at 12 inch standoff).

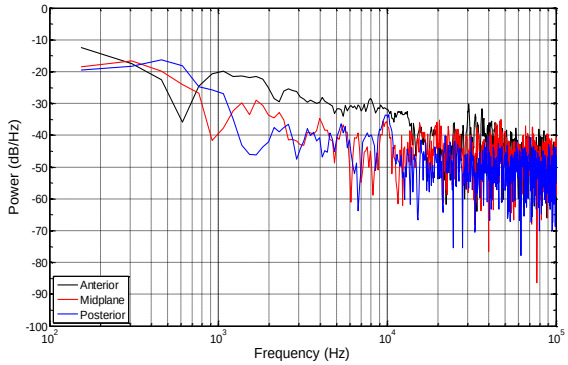

Figure 24: Representative PSD profile of pressure for spherical PMMA shell surrogate head models (model F result shown at 12 inch standoff).

Figure 25. Shadowgraph images of surrogate head model D at 8 inch standoff.

The results of the strain mapping experiments showed successful initial trials. The experiments were performed at the farthest and closest standoff distance to provide a minimum and maximum bound for behaviour. At the 17 inch standoff distance, global target movement was nearly completely eliminated allowing for simple correlation. At the 8 inch standoff distance, the input loading conditions were nearly an order of magnitude larger and therefore some global movement was observed. As a result, the image sequence used for correlation was slightly reduced from the 17 inch standoff distance.

The motion of the Perma-Gel^{TM} that was observed showed significant oscillatory translation in both the vertical and horizontal directions. The maximum displacement measured through the correlation was 5 mm in the horizontal direction and 2 mm in the vertical direction for the 17 inch standoff distance. At the 8 inch standoff distance, maximum values were nearly identical but along opposite directions, most likely as a result of the global movement effect. The maximum shear strain values observed were approximately 3% at the 17 inch standoff and approximately 4.5% at the 8 inch standoff. As would be expected, the largest displacement and shear was often in the middle of the model, farthest from the restrictive boundary of the PMMA ring. However, the location of the maximum values was observed to move around significantly within the model. It can be suggested that the curved surface of the ring (representative of the curved surfaces of the skull) causes transmission angles of the shock wave to vary. As a result, internal shock wave interaction occurs, causing shear and displacement gradients. Furthermore, with gradients occurring, oscillatory rotational movement of the gel (relative to ring and excluding global movement) should be expected due to the varying degrees of displacement between material layers. This rotational movement was in fact observed in the correlation

sequences resulting in the movement of the maximum value locations. Refer to Figure 26 for a representative strain correlation of the analyzed section. The directional arrows specify principal directions.

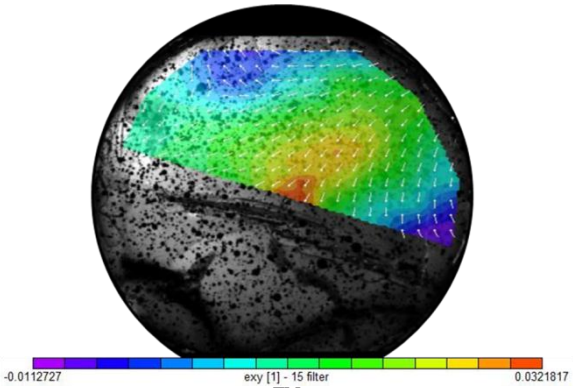

Figure 26. Strain field in Perma-Gel™ at specific time of maximum strain.

An additional feature observed from the strain map imaging was the occurrence of a void creation and collapse event. As stated previously, one possible injury mechanism theory is the occurrence of effects similar to cavitation within the brain[15,16]. Since inertial cavitation is actually the formation of vapor bubbles due to the pressure crossing the vapor pressure limit, it is suggested that technical cavitation is not the true occurrence. Rather, as observed by this strain map imaging, it is suggested that the shock wave transmitting into the tissue (surrogate or biological) causes 3D motion that creates voids by separating tissue interfaces. Immediately following the void creation is the abrupt collapse resulting in locally propagating pressure waves. The consequence of this pressure propagation might be localized pressure of significant magnitude causing additional damage to tissue. In comparison, the strain correlation at the location of the observed void creation and collapse during the event showed highly localized extreme shear values. Therefore, these correlation results assist in validating this theoretical occurrence.

Pressure response of gels from open-field blast experiments

Modeling is simplified somewhat if open field blasts are considered. Open field blast experiments were performed using different surrogate gel materials. Figure 27 shows the comparison of the pressure responses of different gels at a stand-off distance of 30.48 cm. The results in Fig. 27 show a high variability in pressure response near the anterior plane of the simulated head. Furthermore we did repeatability testing to quantify uncertianties for specific gels. Figure 28 shows the pressure response of Perma-Gel™ at a stand-off distance of 30.48 cm. The results of Fig. 28 show repeatability with peak pressures and arrival times both vary in a range of about 10%.

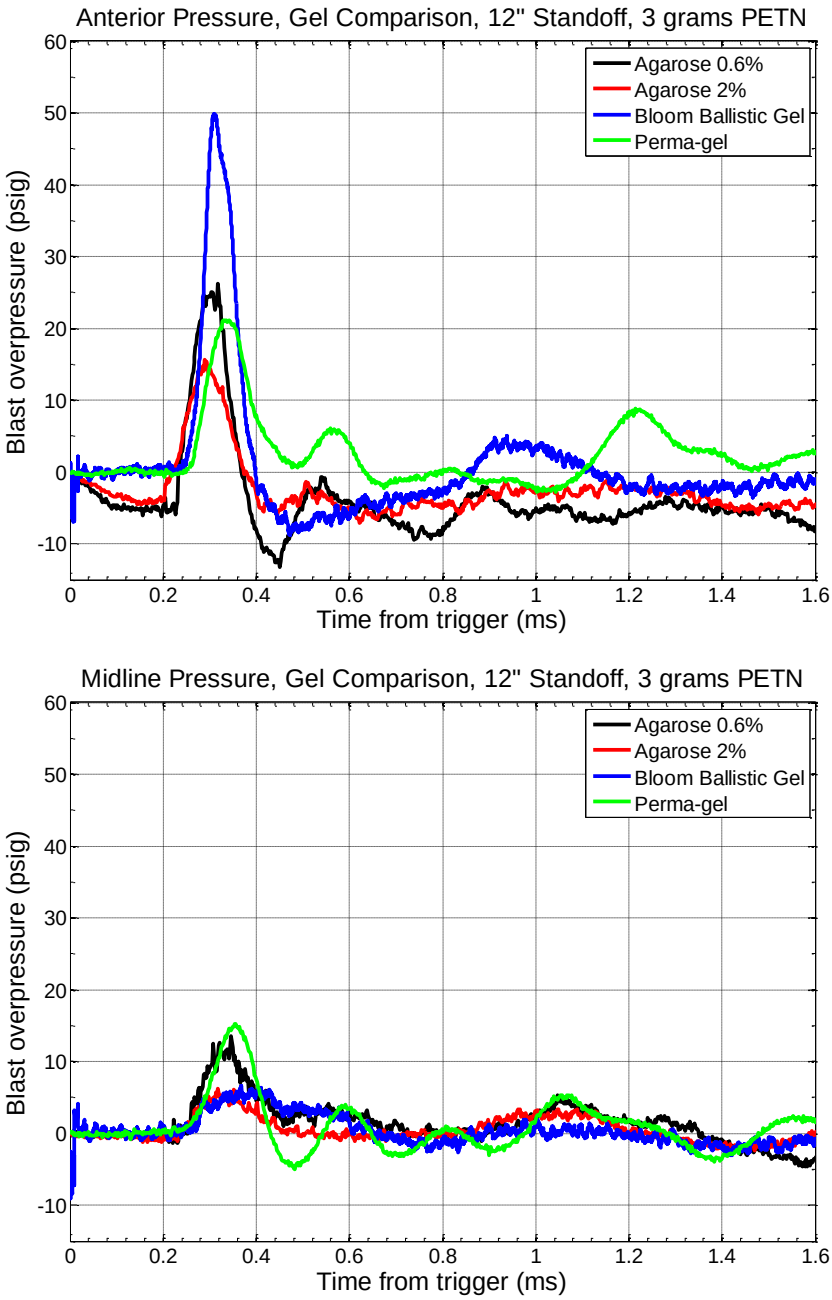

Figure 27: Comparison pressure response of gels under open-field blast conditions

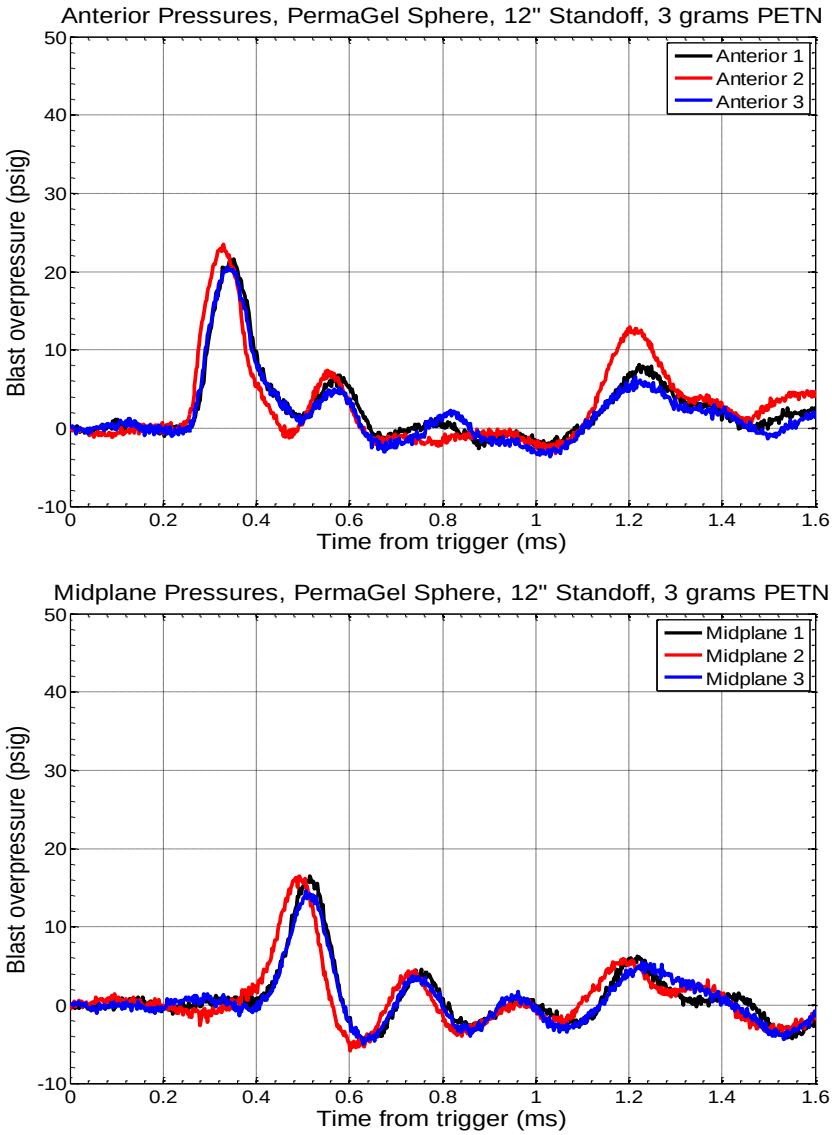

Figure 28: Comparison of pressure responses for Perma-Gel.

Blast Loading Study Conclusions

The goals of this work were to establish systematic methods for laboratory-scale testing of TBI occurrences from IED blasts. In order to accomplish these goals, a uniquely-designed explosive-driven shock tube was utilized to direct and enhance the small-scale blasts. With the shock tube, the laboratory simulated blasts showed profile characteristics similar to those of much larger charges, more closely simulating IED occurrences. The blasts were then directed at surrogate head models by which material variation and geometric features were studied. Internal measurements by instrumentation and imaging provided useful data representing the system response to the blasts. Using these methods, critical factors for experimental modeling and TBI occurrences could be studied. Additionally, since the TBI research area is relatively young, there

is no comparable data currently available showing these effects. Therefore, the data obtained could assist in confirming or developing injury mechanism theories and provide validation for computational and clinical studies.

The surrogate materials used in the experiments provided upper and lower bounds for possible loading behaviour. Although it is impossible to exactly match the human anatomy according to mechanical properties, these types of systems can be developed to provide insight. The accepted mechanical properties of the biological materials of interest were compared to the surrogate materials used. Although there are differences, the biological materials can be placed within the bounds and be expected to exhibit behaviour patterns similar to those seen experimentally. Furthermore, computational models validated to these data could, with higher confidence, be applied to actual head simulations.

The experimental results suggested the importance of material selection coupled with geometry. Behaviour differences were observed with model variation. Pressure amplifications were experienced at the anterior locations near PMMA/gelatin boundaries. The presence of ocular/nasal passages did in fact support the theory of a more direct application of the blast into the cranial cavity, therefore possibly intensifying injury. Global movement of the target was not experienced until a later time, well after initial shock loading and internal response. Furthermore, strain fields calculated internally showed up to 4.5% strain, even with the moderately stiff Perma-GelTM and the highly restricted motion. Additionally, internal tissue displacement results revealed significant tissue movement relative to the shell. Finally, void creation and collapse was observed suggesting the possibility of extreme localized shearing supporting additional possible mechanisms of injury by exceeding material strengths.

References

[1] Bhattacharjee Y. Shell Shock Revisited: Solving the Puzzle of Blast Trauma. Science 2008:406-408.

[2] Warden D. Military TBI During the Iraq and Afghanistan Wars. Journal of Head Trauma Rehabilitation 2006;21(5):398-402.

[3] Taber K, Warden DL, Hurley RA. Blast-related traumatic brain injury: What is known? Journal of Neuropsychiatry and Clinical Neurosciences 2006;18(2):141-145.

[4] Wilson C. Improvised explosive devices (IEDs) in Iraq and Afghanistan: Effects and countermeasures. In: CongressionalResearchService, editor. Washington, DC: The Library of Congress; 2007.

[5] Casualty Summary by Reason Code. In: DepartmentOfDefense, editor. Defense Manpower Data Center; 2008.

[6] Fischer H. United States Military Casualty Statistics: Operation Iraqi Freedom and Operation Enduring Freedom. In: CongressionalResearchService, editor. Washington, D.C.: The Library of Congress; 2008.

[7] DePalma RG, Burris DG, Champion HR, Hodgson MJ. Blast Injuries. New England Journal of Medicine 2005;352(13):1335-1342.

[8] Okie S. Traumatic Brain Injury in the War Zone. New England Journal of Medicine 2005;352(20):2043-2047.

[9] Blast injuries: Essential facts. Center for Disease Control and Prevention; 2006. 2 p.

[10] Courtney A, Courtney M. A thoracic mechanism of mild traumatic brain injury due to blast pressure waves. Medical Hypotheses 2009;72(1):76-83.

[11] Chavko M, Koller WA, Prusaczyk WK, McCarron RM. Measurement of blast wave by a miniature fiber optic pressure transducer in the rat brain. Journal of Neuroscience Methods 2007;159(2):277-281.

[12] Taylor PA, Ford CC. Simulation of early-time head impact leading to traumatic brain injury. Brain Injury 2007;2007(1):7.

[13] El Sayed T, Mota A, Fraternali F, Ortiz M. Biomechanics of traumatic brain injury. Computational methods in applied mechanics and engineering 2008;197:4692-4701.

[14] Halabieh O, Wan JWL. Simulating Mechanism of Brain Injury During Closed Head Impact. Lecture Notes in Computer Science. Volume 5104/2008. Springer Berlin/Heidelberg; 2008. p 107-118.

[15] Mayorga MA. The pathology of primary blast overpressure injury. Toxicology 1997;121(1):17-28.

[16] Ziejewski M, Karami G, Akhatov I. Selected biomechanical issues of brain injury caused by blasts. Brain Injury Professional 2007;4(1):10-15.

[17] Wang Z, Liu Y, Lei D, Bai Z, Zhou S. A new model of blast injury from a spherical explosive and its special wound in the maxillofacial region. Military Medicine 2003;168(4):330-332.

[18] Yilmaz S, Pekdemir M. An unusual primary blast injury: Traumatic brain injury due to primary blast injury. American Journal of Emergency Medicine 2007;25(1):97-98.

[19] Stewart C. Blast Injuries. Colorado Springs: USAF Academy Hospital; 2006. 88 p.

[20] Cernak I, Wang Z, Jiang J, Bian X, Savic J. Cognitive deficits following blast injury-induced neurotrauma: possible involvement of nitric oxide. Brain Injury 2001;15(7):593-612.

[21] Cernak I, Wang Z, Jiang J, Bian X, Savic J. Ultrastructural and Functional Characteristics of Blast Injury-Induced Neurotrauma. Journal of Trauma: Injury, Infection and Critical Care 2001;50:695-706.

[22] Stuhmiller J, PhillipsIII YY, Richmond DR. The physics and mechanisms of primary blast injury. Conventional Warfare: Ballistic, Blast, and Burn Injuries. Washington, D.C.: Office of the Surgeon General; 1991.

[23] Phillips III YY, Richmond DR. Primary Blast Injury and Basic Research: A Brief History. Conventional Warfare: Ballistics, Blast, and Burn Injuries. Washington, D.C: Office of the Surgeon General; 1991.

[24] Simmonds KE, Matic P, Chase M, Leung A. GelMan: A physical model for measuring the response to blast. The NRL Review 2004;2004(1):156-158.

[25] Roberts JC, Biermann PJ, O'Connor JV, Ward EE, Cain RP, Carkhuff BG, Merckle AC. Modeling nonpenetrating ballistic impact on a human torso. John Hopkins APL Technical Digest 2005;26(1):84-92.

[26] Fournier E, Sullivan D, Bayne T, Shewchenko N. Blast headform development. Defense R&D Canada, Biokinetics and Associates Ltd.; 2007. 56 p.

[27] Zhang J, Yoganandan N, Pintar FA, Son SF, Gennarelli TA. An experimental study of blast traumatic brain injury. 2008; Marco Island, FL. ASME.

[28] Miyazaki Y, Tachiya H, Anata K, Hojo A. Measurement of pressure responses in a physical model of a human head with high shape fidelity based on CT/MRI data. International Journal of Modern Physics B 2008;22:1718-1723.
[29] Kinney GF, Graham KK. Explosive Shocks in Air. New York: Springer-Verlag New York Inc.; 1985.
[30] Cooper PW. Explosives Engineering. New York: Wiley-VCH, Inc.; 1996.
[31] Bowen IG, Fletcher ER, Richmond DR. Estimate of man's tolerance to the direct effects of air blast. Defense Atomic Support Agency; 1968.
[32] Settles G. High-Speed Imaging of Shock Waves, Explosions, and Gunshots. American Scientist 2006:22-31.
[33] Settles G. Schlieren and Shadowgraph Techniques: Visualizing Phenomena in Transparent Media. Adrian RJ, M. Gharib, Wolfgang Merzkirch, D. Rockwell, J.H. Whitelaw, editor.: Springer; 2006.
[34] Radovitzky R. Mechanical Properties Measurements and Blast Loading Experiments on Brains for Model Calibration and Validation. In: Alley M, editor. 2007.
[35] Horgan TJ, Gilchrist MD. Influence of FE model variability in predicting brain motion and intracranial pressure changes in head impact simulations. International Journal of Crashworthiness 2004;9(4):401-418.
[36] MIT TBI Selected Head Material Values. MIT; 2008.
[37] Socrate S. Low strain rate mechanical testing of Perma-Gel™. In: Alley M, editor. 2008.
[38] Prabhu R. Low strain rate mechanical testing of Perma-Gel™. In: Alley M, editor. 2008.
[39] Gilchrist MD, O'Donoghue D, Horgan TJ. A two-dimensional analysis of the biomechanics of frontal and occipital head impact injuries. International Journal of Crashworthiness 2001;6(2):253-262.
[40] 2008. WWW.MATWEB.COM. <HTTP://WWW.MATWEB.COM%3E.
[41] 2008. HTTP://WWW.NLM.NIH.GOV/.
[42] Peters WH, Ranson WF. Digital imaging techniques in experimental stress analysis. Optical Engineering 1982;21(5):427-431.
[43] Chu TC, Ranson WF, Sutton MA. Applications of digital-image-correlation techniques to experimental mechanics Experimental Mechanics 1985;25(3):232-244.
[44] Bruck HA, McNeill SR, Sutton MA, Peters WH. Digital image correlation using Newton-Raphson method of partial differential correction Experimental Mechanics 1989;29(3):261-267.
[45] Moore, D.F , Radovitzky, R.A., Shupenko, L., Klinoff, A., Jaffee M.S., Rosen, J.M., 2008. Blast physics and central nervous system injury. Future Neurology 3(3), 243-250.
[46] Miller, K., Chinzei, K., 1997. Constitutive modeling of brain tissue experiment and theory. Journal of Biomechanics 30, 1115-1121.
[47] Pervin, F., and Chen, W., 2009. Dynamic mechanical response of bovine gray matter and white matter brain tissues under compression. Journal of Biomechanics 42, 731-735.
[48] Pervin, F. and Chen, W., 2011, "Effect of inter-species, gender and breeding on the mechanical behavior of brain tissues," *NeuroImage*, 54, S98–S102.

References

[1] Kristin B. Bernick, Thibault P. Prevost, Subra Suresh, and Simona Socrate. Biomechanics of single cortical neurons. *ACTA BIOMATERIALIA*, 7(3):1210–1219, MAR 2011.

[2] D. F. Moore, A. Jerusalem, M. Nyein, L. Noels, M. S. Jaffee, and R. Radovitzky. Computational biology, modeling of primary blast effect on the central nervous system. *NeuroImage*, 47:T10–T20, 2009.

[3] F. Pervin and W. Chen. Dynamic mechanical response of bovine gray matter and white matter brain tissues under compression. *Journal of Biomechanics*, 42(6):731–735, 2009.

[4] T.P. Prevost, A. Balakrishnan, S. Suresh, and S. Socrate. Biomechanics of brain tissue. *Acta Biomaterialia*, 7:83–95, 2011.

[5] T.P. Prevost, G. Jin, M.A. de Moya, H.B. Alam, S. Suresh, and S. Socrate. Dynamic mechanical response of brain tissue in indentation in vivo, in situ, and in vitro. *Acta Biomaterialia*, 7, 2011.

Brain Tissue Response in vivo

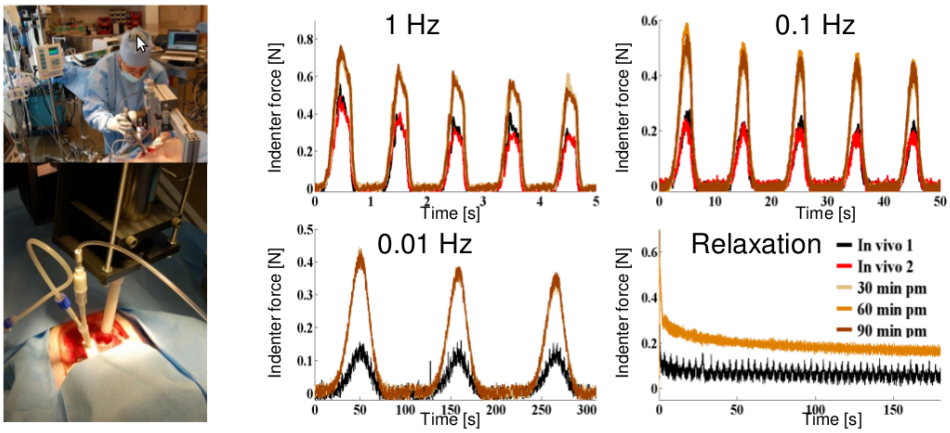

- Tissue significantly stiffer *in situ*
- No *post mortem* time related variations

Figure 4: In vivo vs in vitro tissue response

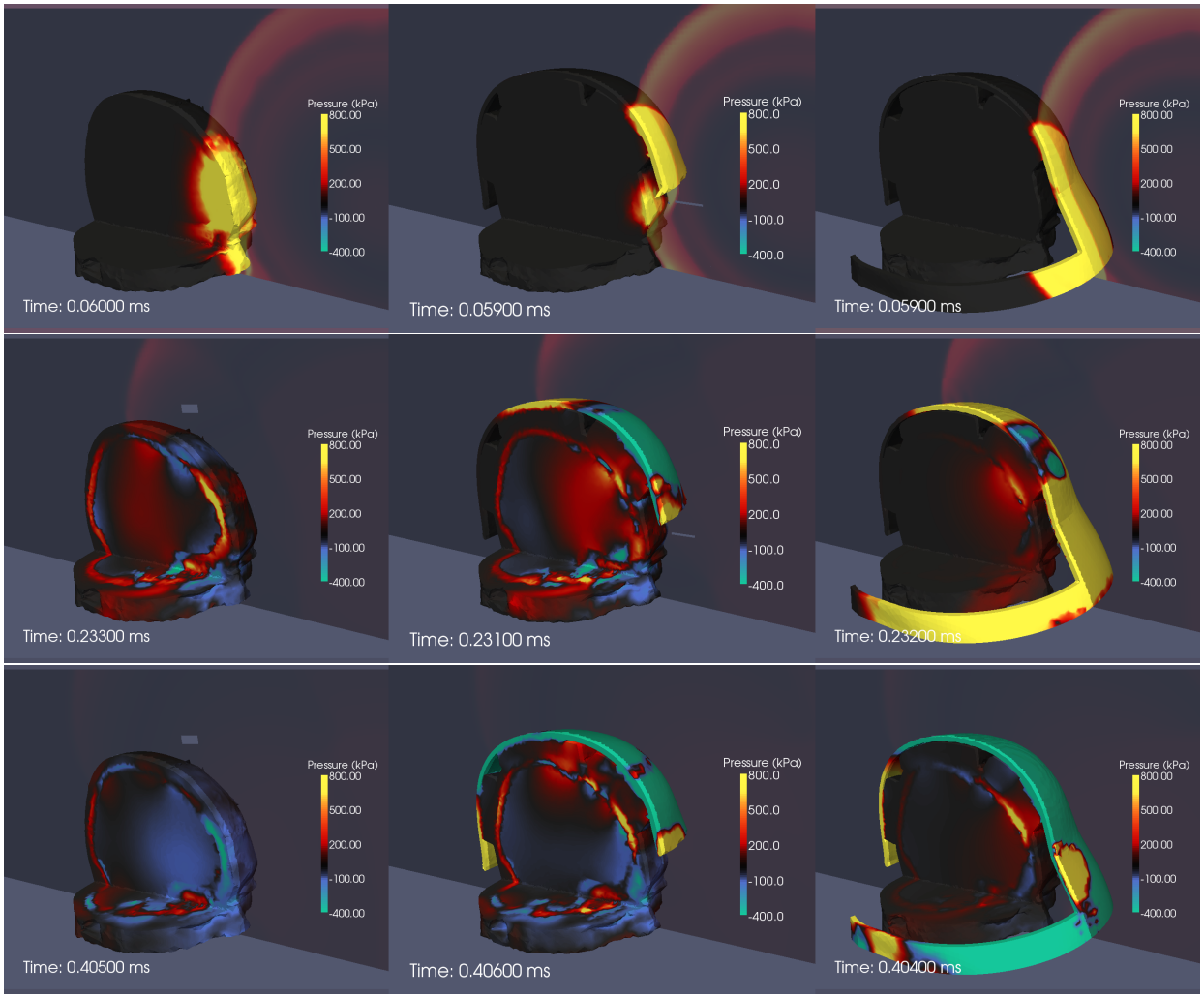

Figure 5: Pressure contours in the head (left column), helmet (center column), and face shield simulations (right column). Starting at the top, the rows correspond to time snapshots at 0.06, 0.23, 0.4 milliseconds. Data at later times excluded from proposal for lack of space. The scale is from -400 to 800 kPa.